Selective thermally oxidised tool surfaces for dry deep drawing

(DFG Grant No. BE 1690/170; MA 1175/41, Funding Period 01.01.2014 – 30.09.2020)

Simon Schöler*[1], Fahrettin Özkaya[2], Christoph Kock[2], Hans Jürgen Maier[1], Bernd-Arno Behrens[2]

[1] Institut für Werkstoffkunde (Materials Science), Leibniz Universität Hannover, An der Universität 2, 30823 Garbsen, Germany

[2] Institut für Umformtechnik und Umformmaschinen (Forming Technology and Machines), Leibniz Universität Hannover, An der Universität 2, 30823 Garbsen, Germany

Summary

Within the scope of German Research Foundation (DFG) Priority Programme (SPP) 1676, this subproject deals with the research of a technology to substitute lubricants in the deep drawing process by selective thermally oxidised tool surfaces. In this context, different atmospheres and methods for selective oxidation of the tool surfaces were investigated. The oxide systems generated were characterised and analysed using high-resolution analysis for examining and classifying their tribological properties [1]. With regard to the layer adhesion and the resulting measurements of coefficients of friction (COF), an α-Fe_2O_3 layer system was chosen, which proved promising for application in deep drawing processes. A special specimen geometry was developed that allows investigation of the tribological wear behaviour of the layer in the deep drawing process. This geometry was intended to mimic the conditions in a deep-drawing process with high cycle numbers of up to 5000 on a laboratory scale and to be suitable for the subsequent analysis methods [2, 3]. The wear specimens were examined on a developed wear test bench and, according to loading cases at dry deep drawing, tested with the sheet metal DP600 + Z under 90° deflection. [4, 5] Based on the results from the wear tests, a numerical FE model was developed capable of simulating the material wear as a function of the process parameters. This served as a numerical tool for predicting layer failure as well as for analysing wear critical areas on the deep drawing tools. In the further course, the heat treatment equipment was upgraded so that samples could be heated inductively in a batch process. This led to increased surface activation and more economical oxidation processes [6]. Since near-surface chromium carbides strongly influence and even prevent selective oxidation, a powder-metallurgically manufactured steel (PM) was also examined. Those surfaces featured chromium carbides in small quantities and to a lesser extent. The selective oxidation of these PM steel surfaces showed excellent results in terms of oxidisability compared to conventionally manufactured steel, as well as constant lower COFs [7]. Following the tribological wear investigations, FE analyses were used to create a modular tool concept enabling the installation of oxidised inserts in defined sections of the tool. After manufacturing, this modular tool was used to validate the applicability of the developed layer system as well as the numerical wear model [8]. In addition to the deep drawing steel DP600 + Z, the electrolytically galvanised deep drawing steel DC04 + ZE was used in these experiments [9]. Tests with both deep-drawing steels demonstrate the good deep-drawability in the dry state with oxidised mould inserts.

Keywords: selective oxidation, dry sheet metal forming, wear testing, surface analysis

1 Introduction and motivation

In order to be able to cope with the growing competitive pressure, today`s industry places high demands on innovative materials. One of the main targets is to reduce friction and wear, as they annually cause enormous

*E-mail address of corresponding author: schoeler@iw.uni-hannover.de

amounts of costs in the manufacturing industry. Increased friction results in more severe forming conditions resulting in poorer formability of the sheet metal in the deep drawing process. This leads to increased component rejects and restricts the possibilities of forming production. The fast and often unpredictable wear leads to frequent maintenance work and thus to expensive production losses. Currently estimated direct losses due to friction and wear are up to 7% of the gross national product in industrialised countries [10]. On this account conditioning of tool surfaces is widely used to reduce wear and optimise friction conditions of forming tools, especially in bulk- and sheet metal forming [11-13]. Usually, liquid lubricating oils are employed in order to increase tool wear resistance and reduce friction. The use of those lubricants, however, has disadvantages, as they contain environmentally harmful additives that are not biodegradable [14-16]. In addition, the use of forming oils can result in longer process chains due to cleaning steps, which has a negative influence on the profitability of the process chain. Dry metal forming could be an alternative to oil based lubrication forming methods. It is defined as "a process where a work piece leaves the forming tool without the necessity of cleaning or drying before further production steps such as coating or joining processes" [16]. In recent works, different approaches for dry metal forming have been investigated [17-23]. In the present study, the potential of selective oxidation of tool steel surfaces as means to realise dry metal forming is investigated.

In general, a metal-metal contact between forming tool and work piece has to be avoided. A better alternative is an oxide-oxide contact, which leads to less adhesion and junction growth [24, 25]. The new approach employed in this project is to generate a thin α-Fe_2O_3 layer on the surface of a hardened tool steel by heat treatment. In this case, an oxide-oxide contact is achieved because the tool-specimen is oxidised and the zinc coating of DP600+Z high strength sheet metal features a native oxide. However, in order to maintain the tool hardness and its geometry, the process temperature must be kept below the annealing temperature of the hardened tool steel so that the tool can be employed directly without any additional mechanical or thermal post processing steps [26, 27].

Positive effects of Fe_2O_3 on the friction and wear behaviour have already been reported earlier. Specifically, these studies addressed the friction and wear behaviour of steel tested without lubrication by means of pin on disc tests with steel pins in the temperature range between 20 °C and 600 °C [13, 14, 21–23]. All these studies showed that the formation of the metal oxide was responsible for the reduction of friction. The oxide, mostly Fe_2O_3, was typically generated from metallic debris during severe wear. In mild wear regimes, oxide removal and new formation were reported to reach a steady-state condition, and thus, friction and wear were at a constant level. At low temperature, the oxides were not beneficial regarding friction and wear behaviour. In [14] it was postulated that this can be attributed to the inferior bonding between oxide particles and of the oxide particles to the substrate at low temperatures. Another proposed aspect was that at higher temperatures plastic deformation occurs earlier. Motivated by the reports about the positive impact of Fe_2O_3 on the friction and wear behaviour [13, 14, 21, 22] further investigations concentrated on the effects of nanometre sized oxide particles introduced into the tribosystem [24–26]. In these studies, a friction reducing oxide layer was formed on the surface by sintering provided that the particles were not oversized.

The base metal can react to four different oxides, namely hematite (α-Fe_2O_3), maghemite (γ-Fe_2O_3), magnetite (Fe_3O_4) and wüstite (FeO). However, the latter is unstable below 570 °C, since it decomposes to α-Fe_2O_3 and Fe_3O_4 [13]. These different oxides can be formed in principle during heat treatment in oxygen containing process gases. The chemical composition and the thickness of the actual layer formed depend on the chosen process parameters. Therefore, especially thick oxide coatings are often composed of distinctive layers with different oxide compositions [14]. A possibility to control the formation and to make the process reproducible is to control the partial pressure of oxygen. At 500 °C, however, the formation of oxide layers on the steel is likely even for small oxygen partial pressures, and thus the process conditions concerning the composition of the atmosphere as well as the temperature-time-regime have to be adjusted properly. However, if the oxides are present in the form of very thin surface films only, the examination of the layers and their composition is difficult, since conventional metallographic analyses of coatings fail at this thickness scale. Surface sensitive methods compatible to the layer thickness are required in this case. In the past, the structure and the composition of oxide layers on metals and semiconductors as well as their formation and reduction behaviour have been investigated intensively using X-ray photoelectron spectroscopy, Auger electron spectroscopy (XPS & AES), scanning electron microscopy techniques (see e.g. [16, 17, 18, 19, 20]) as well as synchrotron techniques (e.g. [21, 22, 23]). In this context, X-ray diffraction is a valuable technique to analyse the crystal structure of the specimens. XRD is surface sensitive by using the total external reflection geometry [24]. For incidence angles below the critical angle of total reflection, the penetration depth of the X-rays is only a few nm and the

reflected beam solely contains information about the near surface region of the specimen. Thus, grazing incidence X-ray diffraction (GIXRD) experiments are well suited for analytical surface investigations in a broad range of scientific fields [25, 26, 27].

From a process engineering perspective the approach proposed in the present study presents new challenges, as the service life of the tools must be re-examined due to the changed wear mechanisms of the dry lubrication layer. However, the advantage of the selectively oxidised α-Fe$_2$O$_3$ layer method is the ability to re-oxidise the tool surface if a critical wear limit has been reached. For the industrial application of the dry lubrication technology, information about the wear behaviour of the layer is essential. On the one hand, the technological implementation of the process is only successful if the tool system does not fail unexpectedly. This results in scrap components and subsequent downtimes of the entire production line. Therefore, to set the service times economically, it is essential to know when a critical wear condition has been reached. On the other hand, an optimised use of the oxidation process requires knowledge of the wear-critical areas on the tools. Using this information, the production process can be improved in a resource-efficient manner by re-oxidising only those tool sections affected by wear.

FE simulation is very helpful for in-depth analysis of forming processes. Particularly, tool life estimation has been gaining importance over the past years. In addition, new challenges in the metal forming industry are high strength materials, the trends towards near net shape production and the demand to increase performance of the forming machines. High strength of the formed material and short cycle times are tightly related to the prevailing contact pressures, and thus to the die load and its final failure due to wear. For the numerical analysis of tool wear, the Archard model [1] is well-established (equation 1-1). Archard has defined the wear volume (W) as a function of load (P) on the contact area, relative sliding distance (L), local surface hardness of the wearing material (H) and wear coefficient (k):

$$W = k\frac{PL}{H} \tag{1-1}$$

This formulation considers the relative movements between tool and work piece along with the local contact pressures. The wear coefficient k is regarded as being constant over the entire service life of the tool. According to [2], the wear rate does not evolve in a linear fashion during tool life. In general, wear rate is changing through three different stages: the early run-in period with an instable wear rate, the middle stage with stable low wear rate and the final stage, which is characterized by accelerated wear (cf. Figure 1). In order to take these stages into account in the simulation, a wear coefficient depending on the loading duration is required.
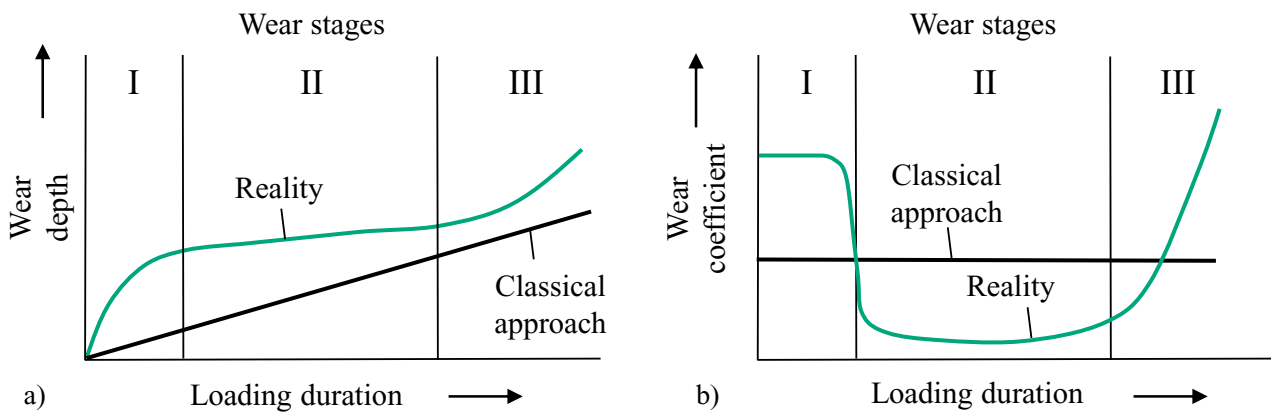

Figure 1: Three stages of wear progress in the course of tool life: wear depth (a) and wear coefficient (b) according to [2].

However, these findings always refer to the wear of tool surfaces in lubricated forming processes. No approaches were available for calculating the removal of oxide layers on tool surface. Therefore, in this subproject of the SPP1676 simulation models with corresponding functions, which allow the calculation of the wear were developed.

In addition to the process parameters while tempering, surface activation is extremely important for selective oxidation. In order to cope with the large number of possible approaches of heat treatment, the oxide formation was investigated in this project using convective as well as inductive heating in stationary and unsteady processes. In addition to the tool steel, which itself poses some challenges while oxidising, there is also interactions with the tribological partner, which influences the wear behaviour. Regarding the tool steel, near-surface chromium carbides, which were created during hardening, proved to be hard to fully cover by oxide layers. In this context, powder metallurgically (PM) manufactured tool steel were identified as a promising alternative, as chromium carbides are less prominent on the surface after hardening. Aiming at the investigation on the tribological wear behaviour of the layer in the deep drawing process, a special specimen geometry was developed. These specimens enabled to mimic the loading and wear situation in a deep drawing process for high cycle numbers of up to 5000 on a laboratory scale. Based on the results from the wear tests, a numerical FE model was developed capable of simulating the material wear as a function of the process parameters. Finally, a modular concept is presented, where the tools are equipped with selectively oxidised inserts. Tests with the deep-drawing sheet materials DP600 + Z and DC04 ZE demonstrated the good deep-drawability in the dry state with oxidised mould inserts.

2   Materials and Methods

2.1 Materials and specimen preparation

In order to gain information about the sliding wear behaviour of the investigated tribo systems, hardened (56 HRC) cylindrical tool steel specimens (EU alloy grade 1.2379 with a chemical composition of 12 % Cr, 1.55 % C, 0.9 % V, 0.8 % Mo, balance Fe, in wt. %, diameter: 16 mm; length: 50 mm)) were designed, cf. Fig. 2 a). After machining, the specimens were polished to an average surface roughness of $S_a = 0.2$ µm using diamond suspension. The geometry was designed to ease non-destructive analysis (small active part), and allow heating (with heating cartridges) and monitoring the temperature with thermocouples, cf. Fig. 2 b) [4, 5].
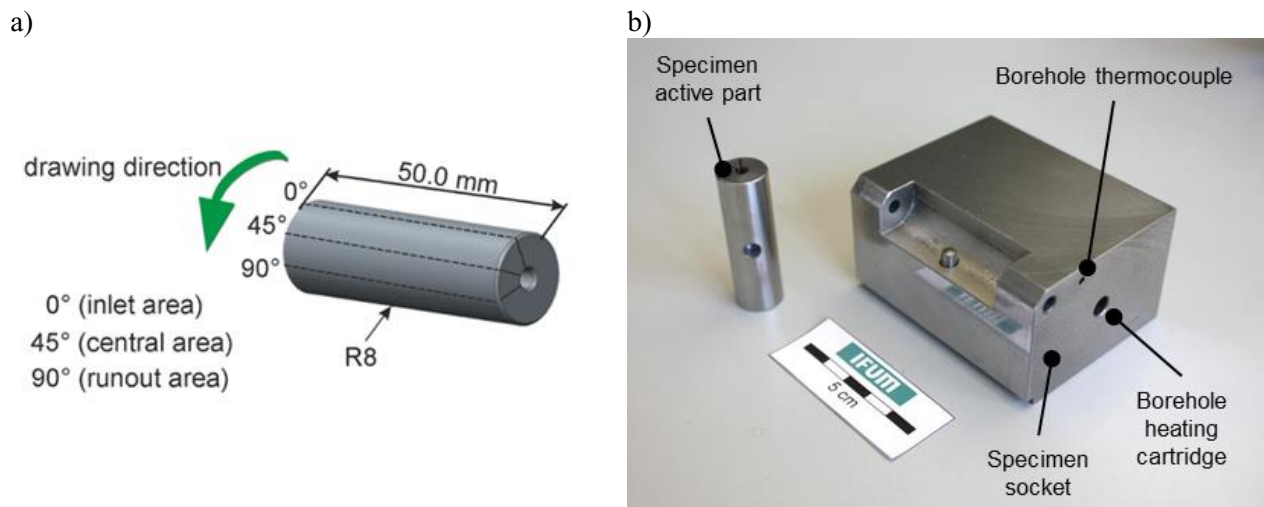

Figure 2: Specimen with marked wear areas (a); wear specimen with specimen holder (b) [57].

In addition to the specimens made from conventional 1.2379 tool steel specimen, powder metallurgically manufactured samples were also prepared. The sheet material used as counterpart for the wear experiments was the dual-phase-steel DP600+Z manufactured by Tata Steel Europe Limited (EU alloy grade 1.0936 with a chemical composition of 2.0 % Mn, 1.5 % Si, 1.0 % Cr + Mo + Ni, 0.14 % C 0.07 % P, min. 0.015 % Al, 0,015 % S and 0.005 % B, balance Fe, in wt. %,). The nominal thickness of the metal strips was 0.96 mm. The strips had a width of 35 mm and were received in a hot-dip galvanised condition with a 9.5 ± 0.5 µm thick Zn coating on each+side. For comparison to the DP600+Z, an electrolytically galvanised deep-drawing steel DC04+ZE was used as well. This sheet material with the EU alloy grade 1.0338 (chemical composition of 0.4 % Mn, 0.03 % S, 0.03 % P and 0.08 % C in wt.- % and balance Fe; thickness: 1 mm) was used in order to evaluate the transferability of the results obtained in the investigations with DP600+Z. For tribometer tests, a disc of conventional austenitic stainless steel (EU alloy grade 1.4301 with an elemental composition of 0.08 % C, 1.0 % Si, 2.0 % Mn, 0.045 % P, 0.03 % S, 19.5 % Cr, 10.5 % Ni, 0.1 % N, in wt. % and balance Fe; diameter: 110 mm; hardness: 32 HRC) was used as the friction counterpart.

Prior to selective oxidisation and all subsequent tests, the specimens were cleaned in an ultrasonic bath with ethanol (> 96.0 %) for 10 minutes. Thereafter, the specimens were rinsed with pure acetone (> 99.5 %) and in a final step with pure ethanol (> 99.8 %). Details of the cleaning procedure can be found in [49]. The cleaning procedure of the drawn sheet metal was realised inline in a cleaning station implemented in the wear test bench as described in detail in [5].

2.2 Methods

2.2.1. Selective oxidation

The sample surfaces were selectively oxidised using different heat treatment concepts. In earlier work [1], the selective oxidation took place in a continuous furnace under defined process conditions. Different oxide systems could be generated, which feature low friction coefficients, but the wear behaviour of these initial layers was unsatisfactory. Thus, in later work, pure α-Fe_2O_3 layers were generated under an inert protective gas atmosphere at a defined oxygen partial pressure using convective and inductive tempering methods. Furthermore, the equipment was expanded and a batch process with inductor was employed (cf. Fig. 3 a)) to realise different heating ramps and associated surface activations, cf. Fig. 3 b).
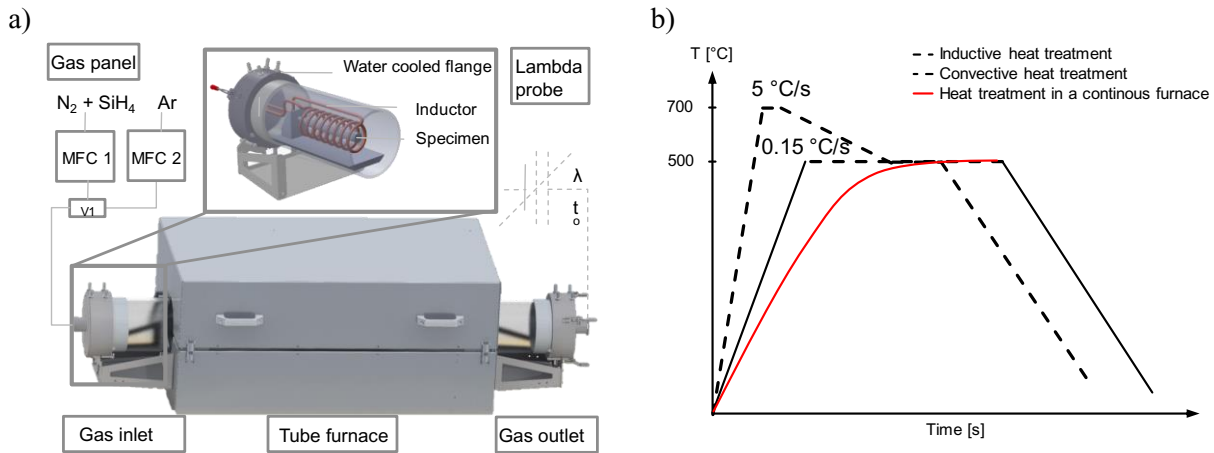

Figure 3: Tubular furnace with inductor and mass flow controllers (MFC) (a) and heating ramps employed for different heat treatments (b)

Details from the experimental set-up can be found in Ref. [6]. Stationary conditions were achieved by controlling the gas flow, the composition of the atmosphere and the process temperature. Argon (Ar) with a purity of 99.996 % was used as inert shielding gas. The heat treatments were conducted for both, wear specimen and reference samples. The inductive heat treatment was performed below the annealing temperature (530 °C) of the tool steel using a constant heating rate of 15 °C/s. The oxygen content was controlled by a lambda probe and kept constant at 0.03 vol.-%. After reaching the target temperature, the specimens were held isothermally for different periods of time prior to cooling down to ambient temperature at a rate of 5 °C/s. The temperature of the specimen was measured during heat treatment using a thermocouple, which was located in a drill hole terminating in the specimens centre. In addition, the inductive heating process was simulated to calculate the temperature distribution within the specimens and the surface temperature, which is crucial for the oxidation process [7].

2.2.2 Surface analysis

The steel surfaces were non-destructively prior to wear testing using grazing incidence X-ray diffraction (GIXRD). For the experiments synchrotron radiation and a PILATUS 100 K detector system [50, 51] at Beamline10 [52] of the DELTA synchrotron Radiation source [53] were employed. Depending on the incidence angle, penetration depth could be set between 250 nm and 4 μm.

In addition, scanning electron microscopy (SEM) in a Zeiss Supra 55 VP was employed for high resolution characterisation of the oxide layers. Chemical composition of selected areas was probed using Energy dispersive X-ray spectroscopy (EDX) allowed probing the local chemical composition. In order to obtain detailed information about layer thickness thin lamellae were cut from the oxidised surface using a focused ion beam (Zeiss Auriga).

2.2.3 Tribological tests

To obtain information on the adhesive strength of the selectively oxidised layers, tests were performed according to VDI guideline 3198 using a standard Rockwell-C hardness tester (Struers – DuraJet). In these tests, a diamond with a 120° point angle (C-cone form) is pressed onto the specimens' surface, inducing a three-dimensional deformation of the substrate. A subsequent optical microscopic (Zeiss Axioplan 2) evaluation was used to assess the adhesion quality of the composite [54].

Tribological tests were performed in a TRM 5000 tribometer (Wazau, Germany) using a pin on disc configuration. The specimen serving as the pin were placed in a socket, and loaded with 500 N at a constant radial sliding speed of 20 mm/s. The tests were conducted without lubrication under dry friction conditions at ambient temperature up to 80 cycles with the disc counterpart made from conventional 1.4301 austenitic steel, which was replaced after every procedure.

The wear tests were performed on a hydraulic wear test bench with 90° deflection. The high strength DP600+Z sheet metal was drawn over the surface of the wear specimen under different loading conditions to investigate the wear behaviour of the tribological system, cf. Fig. 4. The setup is described in detail in [5]. The surface pressure was measured with pressure indicating films between the sheet metal strip and the specimen and was set between 80 MPa and 95 MPa. In order to investigate the friction behaviour of the oxide layers, the number of strokes was varied. For each surface pressure condition, two specimens were tested to 500 and 5000 strokes. Thus, up to 300 m of the material were drawn over the specimen's surfaces. All specimens were tested at 80 °C, which corresponds to the typical average tool temperature in conventional deep drawing processes. In addition to the oxidised specimens, non-oxidised reference specimens were also tested.
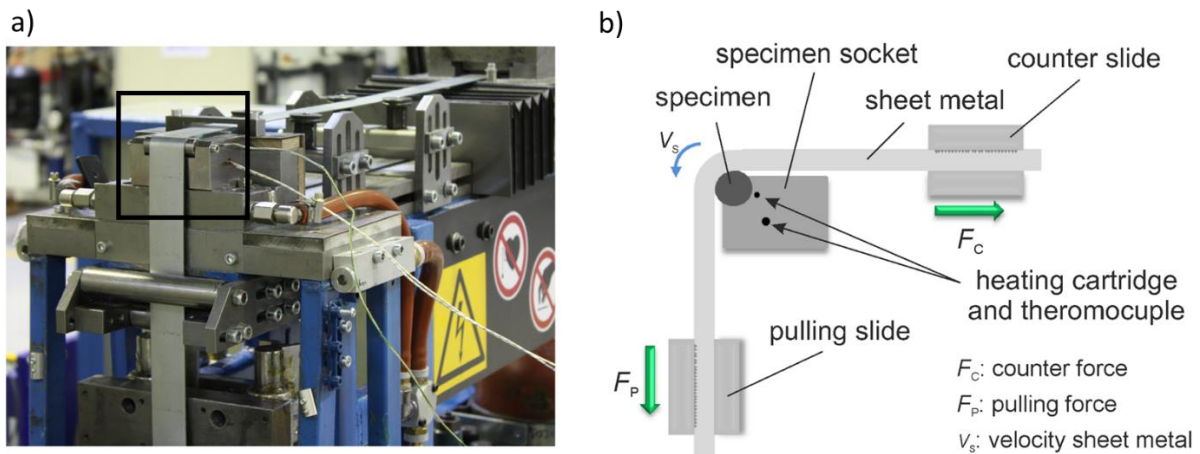

Figure 4: Wear test bench setup (a); principle of the wear test bench (b) [5]

In order to obtain information about the friction behaviour, strip drawing tests were carried out to determine the coefficients of friction between the selectively oxidised tool surfaces and the sheet metal strips of DP600+Z. The strip drawing tests were conducted on an universal test bench, which can be used for experiments without and with deflection. Both variants allow investigating the coefficients of friction of different areas and different load conditions (cf. Fig. 5). While the test without deflection focuses on the flange area of the drawing ring, the test with deflection mimics the area of the drawing edge radius. Flat specimens were used for the test without deflection while cylindrical specimens were used for the test with deflection. The hot-dip galvanised sheet metal DP600+Z with a sheet thickness of 0.96 mm was used for both test variants, which had a length of 1000 mm and a width of 35 mm. To ensure that the tests were carried out in an oil-free and dry condition, the factory oiling of the sheet metal strips was cleaned with a 10 % cleaning solution (Tickopur R33). The tests were carried out at a surface pressure of 18 N/mm^2 and a drawing speed of 20 mm/s. The friction coefficients were determined at a temperature of 100 °C. For this purpose, heating cartridges were used to heat the specimens. The temperature was measured using type J thermocouples, which were integrated into the heating cartridges. The surfaces of the test specimens were processed in different conditions (initial, ground finish with SiC 1000 and polished with diamond suspension) in order to investigate the influence of the surface topography on the growth of the oxide layers and the resulting friction coefficients.
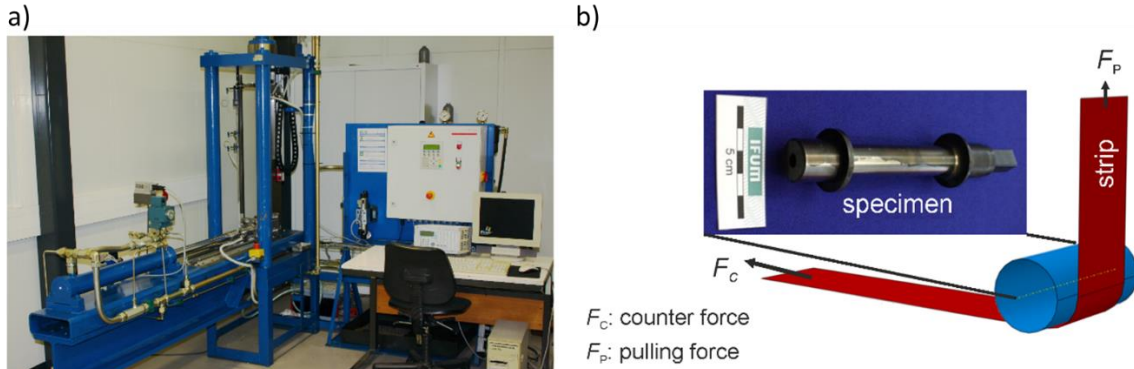
Figure 5: Universal test bench for the determination of friction coefficients (a); specimen and testing concept to determine the friction coefficient with cylindrical specimen for strip drawing tests with deflection (b) [1]

The strip drawing test with deflection was divided in two process steps to determine the bending force during the first and the sliding force within the second process step. This procedure allows the calculation of the friction coefficient using the belt friction law of EYTHELWEIN. The required forces were applied by two hydraulic cylinders mounted on the test bench. The drawing force was generated by the vertical hydraulic cylinder. With the help of the drawing force, the sheet was drawn over the roll with a deflection of 90°. In contrast, the horizontal arranged hydraulic cylinder counteracts the drawing force and generates the counter-force. The resulting surface pressure was derived from these two forces. In the first phase, the cylindrical test specimen, which initiates the deflection of the sheet metal strip, was mounted in the set-up via two ball bearings so that no relative movement between the test specimen and the sheet metal strip occurred. In the second phase, the rotation of the test specimen was blocked by a mechanical locking mechanism. Due to the relative movement between sheet metal and the test specimens' surface, sliding friction occurred and the coefficient of friction could be determined.

In the test variant without deflection flat test specimens were used. The principle of the strip drawing test without deflection is shown in Figure 6. During a test procedure, two pistons were guided hydraulically in a vertical and a horizontal cylinder. On the vertical cylinder, a sheet holder with the sheet metal strip was mounted. The test specimen surface was pressed against the metal strip by the horizontal counterforce and then pulled upwards, resulting in a frictional contact between the two components. To avoid friction between the sheet metal holder and the duct, the sheet metal holder was supported on the back by roller bearings. The coefficient of friction was determined by Coulomb's law using the recorded forces.
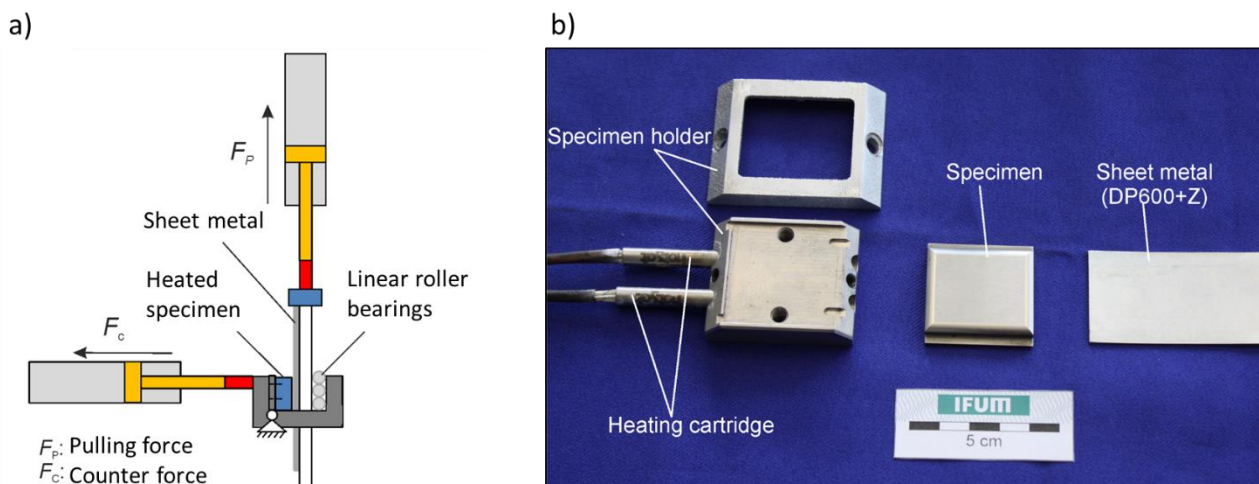

Figure 6: Principle of the strip drawing test setup without deflection (a); Specimen geometry for investigation of friction characteristics on variable surfaces (b)

2.2.4 FE Simulations

2.2.4.1 Thermo-mechanical material characterisation for the numerical wear investigation

A thermomechanical material characterisation was carried out for determination of flow curves and anisotropy parameters of the sheet materials DP600+Z and DC04+ZE being used in this project. During the manufacturing process, the average temperatures of the deep-drawing tools and the sheet materials were between 80 and 120 °C due to the released heat as a result of plastic deformation. Therefore, isothermal tensile tests at temperatures of 20 °C, 80 °C and 120 °C were conducted using a quenching and deformation dilatometer (DIL805 A/D+T from TA Instruments).

2.2.4.2 FE simulations of strip drawing wear tests and deep drawing processes

The simulations in this study were performed with the commercial FE software Abaqus CAE 6.14-2. Both strip drawing tests with deflection and deep drawing processes were simulated according to the experimental boundary conditions. Strip drawing tests were simulated in order to determine whether the wear coefficient is cycle number dependent. The process simulation of deep drawing was carried out to verify the applicability of the developed wear function to a complex deep drawing process. Information on the modeling and the properties of the wear function are given in chapter 3.4.

3 Results and discussion

3.1. Surface characterisation of reference sample surfaces prior to the tribological investigations

3.1.1 GIXRD

The surfaces were analysed by GIXRD in order to investigate the crystallographic and chemical changes occurring. Depth resolved information was obtained by the collection of diffraction patterns at various incident angles. When an oxide is present on the surface of the sample, the diffraction pattern is a superposition of both oxide and metal diffraction peaks, and the metal (substrate) contributions are damped in intensity by the presence of a surface oxide. For small incidence angles, the surface components are dominant while the bulk material becomes prominent for higher incidence angles. In Fig. 6 a) grazing incidence X-ray diffraction spectra of different heat-treated samples (510 °C and 0.03 vol.-% oxygen content) and a native reference sample are shown. 2D GIXRD patterns for an incident angle of $\Theta = 1.6°$ are recorded and shown in Fig. 7 b). Each pattern shows a major reflex at about 35.5° that can be clearly assigned to α-Fe. The reflex at about 31.3° can be attributed to Cr_7C_3. The heat-treated samples showed a couple of additional reflexes, which all could be assigned to Fe_2O_3. The reflexes at 19.4°, 26.5° and 32.6° belong to α-Fe_2O_3. The reflex at 28.5° can be attributed to two species of Fe_2O_3 (α-Fe_2O_3 and γ-Fe_2O_3). The dominate component must be α-Fe_2O_3, because no additional single γ-Fe_2O_3 reflex could be detected. The intensities of all α-Fe_2O_3 reflexes are decreasing with higher incident angles, and thus, the iron and oxygen rich layer (see Fig. 7 b) consists mainly of α-Fe_2O_3.
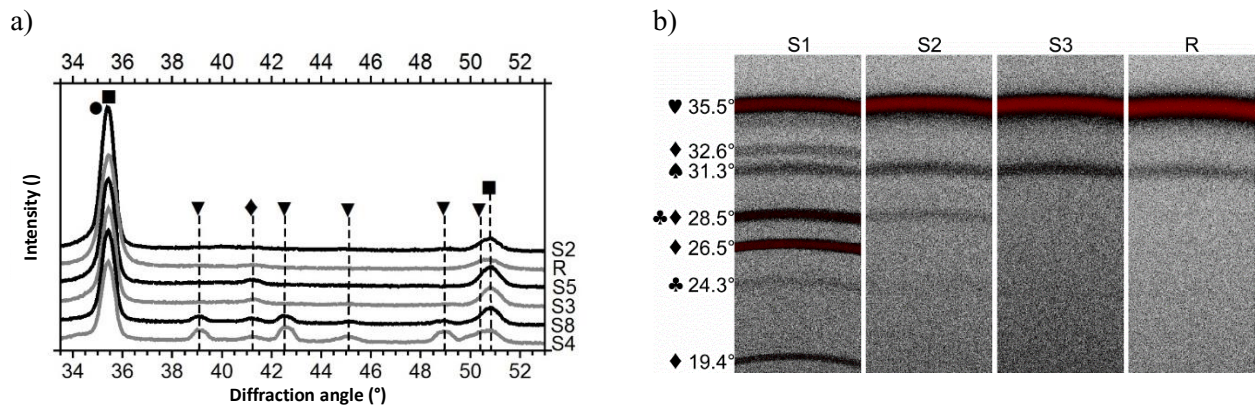

Figure 7: Grazing incidence X-ray diffraction spectra of different heat treated samples: α-Fe (■), Cr (●), α-Fe_2O_3 (▼) and Cr_7C_3 (♦) (a); 2D GIXRD recording (angle of incidence $\Theta = 1.6°$) α-Fe (♥), α-Fe_2O_3 (♦), Cr_7C_3 (♠) and γ-Fe_2O_3 (♣) (b) [1, 5].

3.1.2 SEM analysis prior to tribological investigations

Information about the morphology and the chemical composition of the surface system were obtained by different surface sensitive analytical methods. Reference samples heat-treated in a nitrogen atmosphere at 500 °C, i.e. under conditions employed for the actual wear specimens, were used for characterisation of the oxide layer. The geometry chosen for the reference samples (material: 1.2379, hardness: 56 HRC, diameter: 12 mm, height: 2 mm, surface polished with 3 mm diamonds) allowed for a direct analysis without any artefacts caused by metallographic preparation. A secondary electron image of the oxide formed on a reference sample is shown in Fig. 8. The structure is not completely uniform. In order to obtain further insight, cross sections were prepared using a focused-ion beam. The region selected was coated with a platinum layer to protect the oxide.
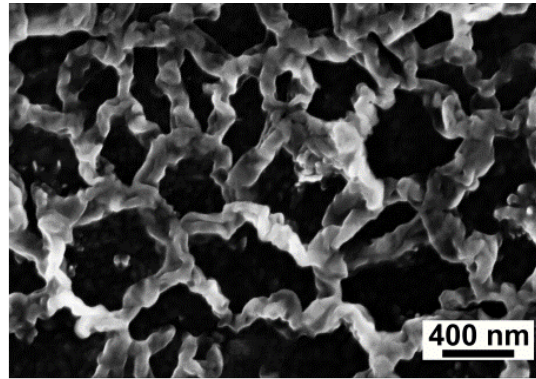

Figure 8: SEM image of an oxide formed on a reference sample using an inlens detector [5]

3.1.3 Focussed ion beam cutting

The selectively oxidised specimen surfaces of the tool steel investigated have been characterised as α-Fe_2O_3 layers by GIXRD as described in section 3.1.1 and in more detail in Ref. [5]. Selective oxidation was realised under conditions (510 °C and 0.03 vol.-% oxygen content) so that stable generation of α-Fe_2O_3 layers resulted. Figure 9 a) shows a secondary electron image of a selectively oxidised specimen surface (hardened; conventionally manufactured). As already shown in Fig. 8 the structure of the oxide layer is not completely uniform and the surface had not been oxidised in chromium rich areas, while a homogeneous layer of α-Fe_2O_3 formed outside these regions. Chromium carbides seem to have coarsened in the course of hardening, such that the interconnection of the chromium carbides maximises the size of features that are not oxidised.
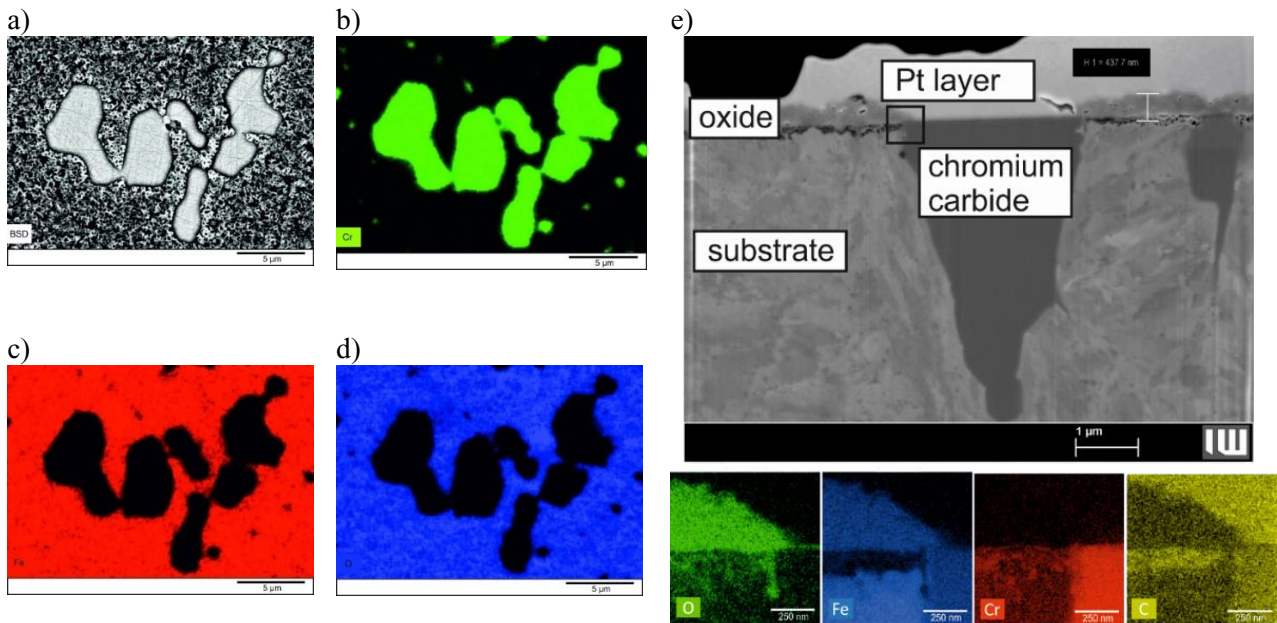

Figure 9: EDX mapping of a specimen surface after selective oxidation prior to the tribological investigations: backscattered electron (BSE) image (a). Cr elemental mapping (b). Fe mapping (c). O mapping (d). Secondary electron (SE) image of a cross section prepared by focussed-ion beam cutting of a lamella (e). The elemental mappings shown underneath the SE image were obtained from the region marked by the black rectangle in e) and recorded at 15 keV [7]

A lamella prepared using focussed ion beam (FIB) cutting from a hardened conventionally manufactured specimen's surface provided high-resolution information about selective oxidation by decreasing the x-ray emitting volume substantially. Fig. 8 e) shows the generated layer with a thickness of about 440 nm, while an EDX mapping of the cross section demonstrates the different oxidation states. Specifically, the EDX mapping of oxygen documents that selective oxidation of larger chromium carbides could not be realised, but is possible for smaller ones. In addition, the grain boundary between carbides and substrate seems to be energetically favourable for internal grain boundary oxidation. Moreover, the oxide layer is rich of iron and oxygen, while the reaction zone beyond the oxide layer at the substrate edge features a very low signal of iron. Based on these insights the diffusion rate of iron from the substrate edge to the oxide layer seems to be higher than from the bulk to the substrate edge.

3. 2 Analysis of inductively tempered PM Steel surfaces

In an effort to avoid large near-surface chromium carbides, which obviously inhibit selective oxidation, PM steels were analysed and evaluated with regard to their oxidation behaviour in comparison to conventional manufactured tool steel specimen.

3.2.1. SEM analysis of reference sample surfaces

In order to evaluate the influence of surface activation in context of the different heat treatment methods and durations on the morphology of the generated oxide layers, secondary electron images were recorded at a low acceleration voltage of 4 kV for different specimen conditions (Fig. 10). Large areas that have not been oxidised were detected for oxidised surfaces of conventionally melted specimen surfaces, while the oxide layer seem to have coarsened for extended dwell times, cf. Fig. 10 a) and 10 c). In contrast, chromium carbides are much more finely distributed at the surfaces of PM specimen surfaces and occupy are smaller surface area (Fig. 9 a) and 9b). The optical contrast of morphological oxide structure is more intense for surfaces that have been oxidised for an extended heat treatment duration of 30 minutes, indicating that the oxide layer gets thicker.

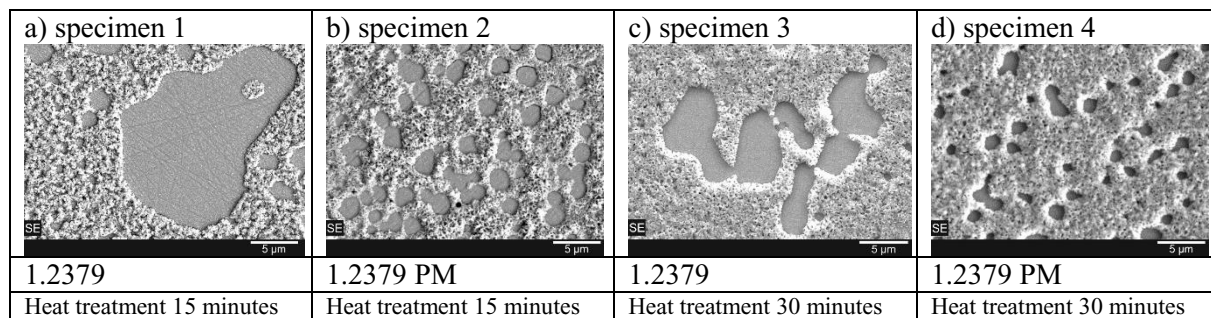| a) specimen 1	b) specimen 2	c) specimen 3	d) specimen 4
1.2379	1.2379 PM	1.2379	1.2379 PM
Heat treatment 15 minutes	Heat treatment 15 minutes	Heat treatment 30 minutes	Heat treatment 30 minutes

Figure 10: Secondary electron images of 1.2379 tool steel surface tempered for 15 minutes (a), 1.2379 PM tool steel surface tempered for 15 minutes (b), 1.2379 tool steel surface tempered for 30 minutes (c), 1.2379 PM tool steel surface tempered for 15 minutes (d) [7]

3.2.2. Rockwell-C tests

In order to obtain information about the adhesive strength of the generated oxide layers a standard Rockwell-C hardness tester was used. Different damage stages were compared with the adhesion strength quality maps HF1-HF6, which define sufficient (HF1-HF4) and insufficient adhesion (HF5 and HF6) [54]. Figure 10 shows the indents for hardened specimen 1 – 4. For specimen 1, radical cracks at the perimeter of indents with small flaking areas can be indicated. For specimen 3 a congruent failure can be detected, but with a smaller deformation zone and cracking areas at a lesser extent. The PM-manufactured specimen 2 and 4 showed different adhesive behaviour with no cracking and small flaking areas between deformation zone and substrate. For specimens that were selectively oxidised for 30 minutes, specimen 4 showed excellent adhesion behaviour. Adhesion strength quality is summarised in Fig. 11 based on the indention failure map. PM manufactured steel surfaces seem to have the highest adhesive strength after a heat treatment duration of 30 minutes.
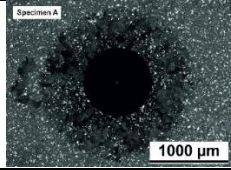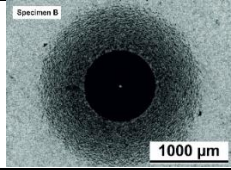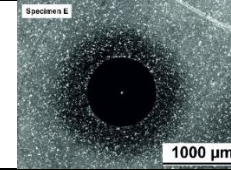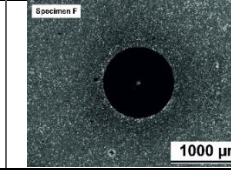
specimen	1	2	3	4
VDI 3198 Rockwell-C indentation failure map	HF4-HF5	HF2	HF3	HF1
	1.2379	1.2379 PM	1.2379	1.2379 PM
	Heat treatment 15 minutes	Heat treatment 15 minutes	Heat treatment 30 minutes	Heat treatment 30 minutes

Figure 11: Light microscopic images of indents on specimen surfaces after Rockwell-C indentation failure tests [7]

3.2.3 Tribometer tests of reference samples

Tribological investigations for PM tool steel surfaces and conventional melted ones were carried out for a normal load of 500 N at a constant radial sliding speed of 20 mm/s. The coefficient of friction was recorded as a function of time at a given normal force (Fig. 12). As seen in Fig. 12 a), an adhesion peak occurred after ≈ 200 s, indicating a collapse of the layer during testing of specimen 1. The powder metallurgical manufactured specimen 2 showed a nearly constant friction coefficient of 0.12, but finally also collapsed at the end of the test after 80 cycles of load, cf. Fig. 12 b).
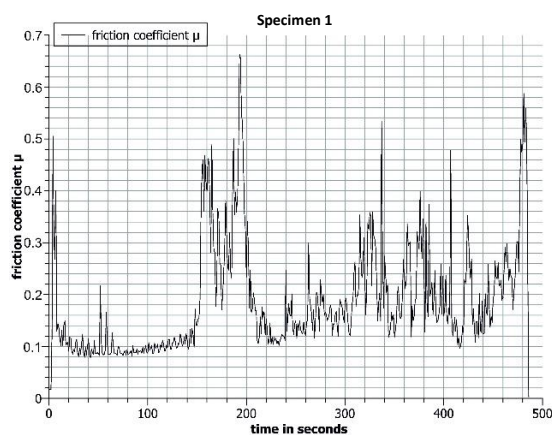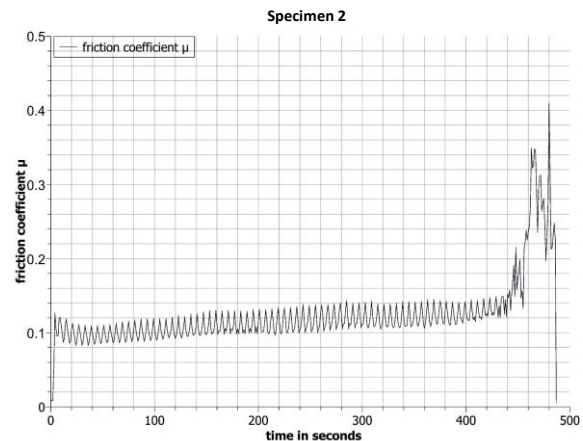

Figure 12: recorded COF for specimen 1 (a); [7]   recorded COF for specimen 1 (b) [7]

3.3. Analysis after wear investigations

3.3.1 Optical 3D-topography of wear specimen

The arithmetic mean height of the wear specimens was measured to investigate the change of surface properties before and after the wear tests. For this purpose, defined areas of the wear test specimens were optically measured at 40 x magnification. For statistical reasons, five measurements with a measuring field size of 5 mm x 2 mm were performed for each test specimen and a high-pass filter $\lambda_c = 0.8$ was selected. Figure 13 shows the arithmetic mean height value S_a of the wear samples before and after the wear tests.
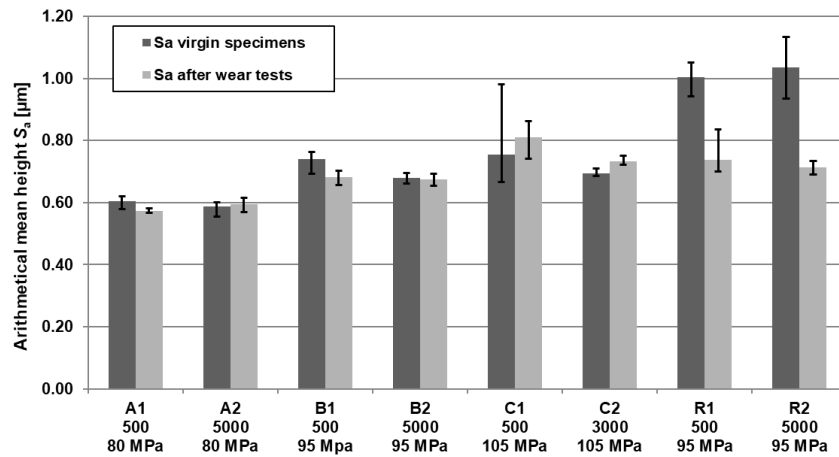
Figure 13: Arithmetical mean height S_a before and after wear tests for each type of specimen; the number of strokes and the average surface pressure is shown below the specimens. [5]

From Fig. 13 it is clear that the S_a-values of the oxidised test specimens before the wear tests are significantly lower in comparison to the unworn reference R1 and R2. Based on the results, a smoothening of the specimen surface occurred due to the formed oxide layer. Differences in the S_a-values of the unworn oxidised test specimens can also be seen. The different S_a-values are due to different surface conditions in the initial state of the test specimens and not due to an error in the oxide layer generation. The results of the 3D-profilometer tests showed that no significant changes in the arithmetic mean height of the oxidised test were present after the wear tests. A slight increase of the S_a-values was observed for the test series C. In contrast, a significant reduction in the S_a-values was observed for the reference specimens R1 and R2. Two mechanisms may be the reason for such a decrease of the S_a-value. On the one hand, the resulting surface pressure smoothens the non-oxidised test specimen surfaces; on the other hand, a significant amount of zinc was transferred from the sheet material to the test specimen surface.

3.3.2 Strip drawing tests of wear specimen

In order to analyse the influence of the process condition on the friction behaviour. Strip drawing tests were conducted. The results of the strip drawing tests with and without deflection for the different surface topographies and specimen conditions are shown in Fig 14.
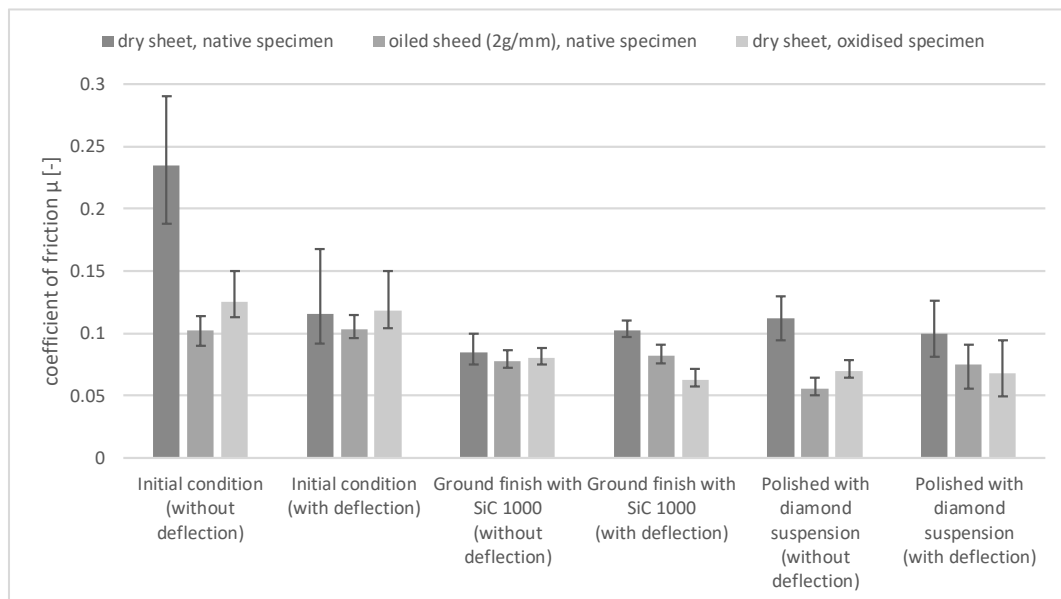

Figure 14: Results of the strip drawing tests with and without deflection for the different surface topographies and specimen conditions

The results of the strip drawing tests show significant differences in the coefficients of friction for all specimen conditions. A similar trend can be observed for both test methods. The highest average coefficients of friction were achieved with dry sheets and the non-oxidised reference test specimen in the test method without deflection. The relatively high coefficient of friction between the dry sheet metal and the non-oxidised reference test specimen seems to be caused by a tilting of the test specimen. In this combination, a strikingly high scattering in the measured values is also apparent. The lowest average coefficients of friction under all conditions were achieved for the most part by the combination of oiled sheets and reference test specimens. However, in a few cases the combination of oxidised test specimens and dry sheets provided better coefficients of friction than the oiled variant. It can be stated that the oxidised test specimens in combination with the dry sheets have similar frictional properties to those of the oiled specimens. The similar friction coefficients are attributed to the oxide layer, which acts as a separating layer between the surface of the test specimens and the sheet metal strip. By using the oiled sheets, the oil acts as a separating layer between the two contact surfaces. In both variants, unwanted direct steel-on-steel contact is avoided, which can also be seen in the low coefficients of friction. The coefficients of friction of the oxidised test specimens with dry sheets and the combination of reference test specimen with oiled sheets appear to be similar for all conditions. A significant difference is not evident. It can be seen that the use of suitable oxide layers can decrease the coefficient of friction and therefore have a positive influence on the friction behaviour.

The coefficients of friction of polished surfaces in combination with dry sheets and reference specimens are substantially higher than those of ground specimen surfaces. The increased coefficients of friction of the polished specimens could be caused by the change in true contact area, which is increased for finer surfaces. The reduction of the protruding peaks on the surface seems to have a significant influence on the sliding resistance and thus on the frictional properties. Based on these results, a ground finishing of the oxidised forming tool surfaces seems to be sufficient with regard to the frictional properties, which is also beneficial from an economic point of view in comparison to fine machining of the surfaces.

In contrast to the results of the strip drawing tests without deflection, lower coefficients of friction were achieved in the tests with deflection for the oxidised specimens in the ground finish and polished condition, irrespective of the topography. Differences in the coefficients of friction between the two test variants are probably due to the way the surface pressure was applied to the contact surfaces. While in the test without deflection, the contact surfaces were flat on top of each other, in the test with deflection the active surfaces were in the radius area. It cannot be ruled out that during the deflection, the applied oil was pressed out of the contact surfaces between the sheet surface and the sample surface. This can explain why the oiled samples have slightly higher coefficients of friction than the dry samples.

3.3.3 SEM analysis following the tribological investigations

To identify the operating wear mechanisms, the wear behaviour of non-oxidised tool steel specimen was investigated. Table 1 summarises the test conditions employed in these tests. Looking at the behaviour of the reference specimens, which have not been oxidised, it can be seen in Fig. 15 that zinc pickup occurred after 500 strokes (specimen *R1*). Quantitative spectrometry revealed that the zinc transfer occurred preferentially at the location of large chromium precipitations present at the surface (cf. Fig. 15). Thus, chromium precipitates not only pose a challenge in oxidizing the tool steel surface, but also promote zinc transfer from the sheet to the test specimen. In essence, the carbides act as hard abrasive surface defects that break out parts from the relatively soft hot-dip galvanized sheet metal. The BSD image (Fig. 15 a) shows a picked up zinc particle of about 30 µm in length. The quantitative spectrometry of specimen *C* did not reveal any zinc removal to the specimen's surface (cf. Fig. 16). On the other hand, the surface showed large amounts of chromium precipitates that were non-oxidised like the surface of specimen *R*. In the BSD image, narrow grooves in the drawing direction are visible, suggesting a levelling of the oxide layer.

Table 1: Test parameters used in the wear tests

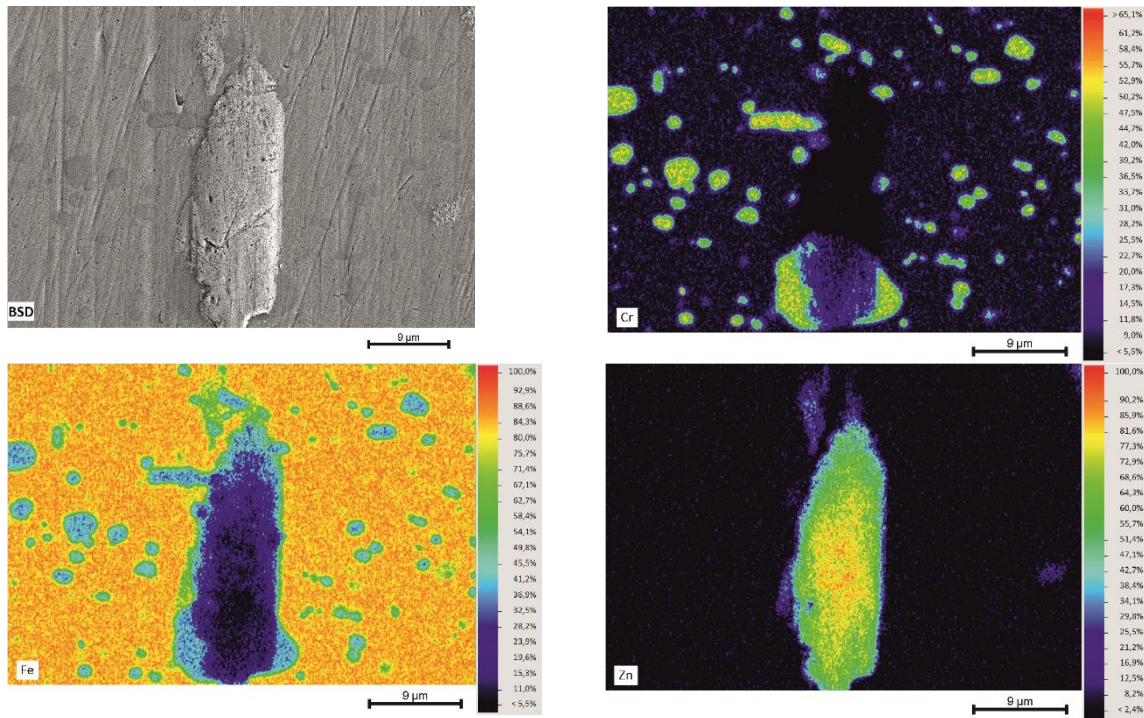| Specimen	A	B	C	D	E	F	R	R1
Strokes of load	0	100	500	1000	2000	500	0	500
Contact pressure [MPa]	-	80	80	80	80	95	-	80
Oxide layer system	α-Fe_2O_3	α-Fe_2O_3	α-Fe_2O_3	α-Fe_2O_3	α-Fe_2O_3	α-Fe_2O_3	-	-

Figure 15: Backscattered electron image of the non-oxidised specimen surface R1 (BSD); quantitative spectrometry data of chromium (Cr), iron (Fe) and zinc (Zn) [8]
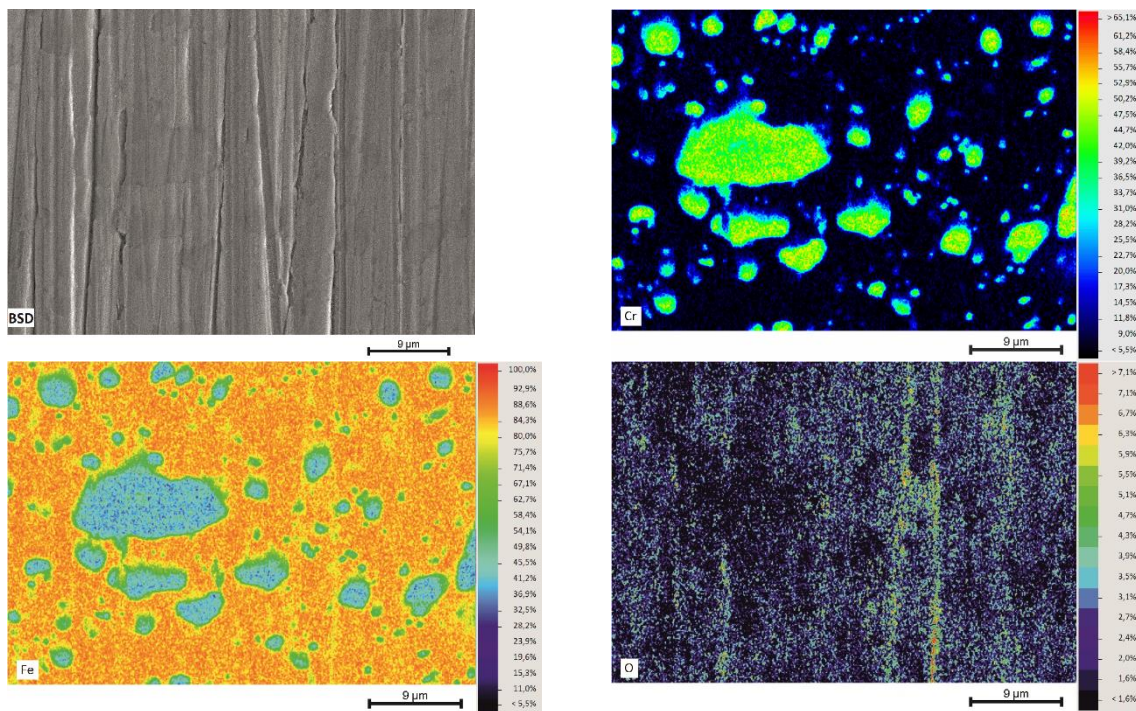

Figure 16: Backscattered electron image of the oxidised specimen surface C (BSD); quantitative spectrometry data of chromium (Cr), iron (Fe) and oxygen (O) [8]

3.3.4 Light microscopy, SEM and optical 3D topography of the sheet metal

After the wear tests, selected parts of the DP600+Z sheet metal were cut out to investigate the interaction between both tribo partners. First, surfaces were analysed by 3D microscopy. Subsequently, SEM images were collected prior to preparation for cross sectional light microscopic analysis. Figure 16 shows images of initial sheet metal strips (left), specimen surfaces of strips after 500 strokes (middle) and after 1000 strokes (right). 3D microscopic images are shown on top; cross sections imaged by light microscopy in the middle and SEM images at the bottom. In the initial state, the zinc on of the sheet metal appears as an insular flaked surface. Both, the SE image and the light microscopic image show clear gaps between zinc areas. The 3D surface image

appears homogeneous with slightly appearing bumps. After 500 strokes the 3D image shows a larger area that seems to have been worn, while areas around appear unaffected. The SE image shows that zinc areas have been smoothened. Grooves are visible on several insular areas, while others appear identical to their initial state. In the light microscopic cross section, the gaps between the zinc flakes disappeared and the surface has smoothened. There is a visible pickup, probably a part of the oxide, which has been broken out of the specimen's surface. The zinc coating is slightly deformed under the pick-up. After 1000 strokes, the sheet metal surface features defects, which can be detected using 3D microscopy (Fig. 17, top right). In addition, the cross section reveals large particles that have been picked up by the sheet metal. The SE image shows that the initial surface structure is completely deformed after 1000 strokes. The entire surface features horizontal grooves that represent the drawing direction.
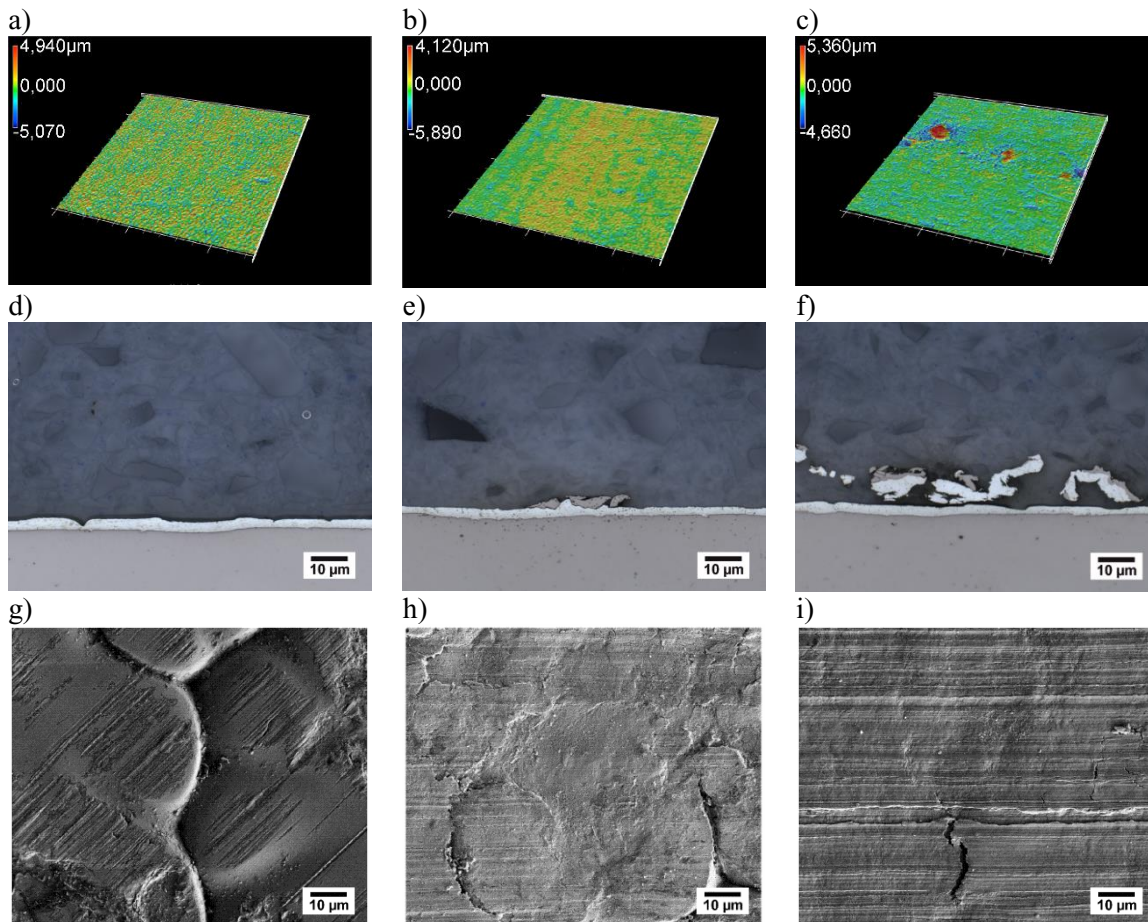

Figure 17: Optical 3D topography of sheet metal surfaces (a-c), light microscopic images of prepared cross sections (d-f) and secondary electron images of sheet metal strip surfaces (g-i) for different loading conditions: 0 strokes (left), 500 strokes (middle) and 1000 strokes (right) [8]

3.4 Development of a numerical FE model for wear prediction

In order to model the wear behaviour of the oxide layer, the analytical results of the specimens from the wear test bench were used. For these wear tests, cylindrical specimens were selectively oxidised (cf. section 2.2.1). Subsequently, the specimens were subjected to strip drawing tests with deflection, whereby a strip of sheet metal were drawn 60 mm along 45° of the circumference of the specimen in each cycle (cf. section 2.2.3). This model-test is particularly suitable for determining the removal behaviour of the oxide layer, since the rounding of the specimen leads to the similar loading conditions as those that prevail on the drawing ring in industrial deep drawing processes.

In the classical tool analysis, it is assumed that the wear is directly proportional to the local surface pressure and the relative speed of tool and work piece as well as inversely proportional to the hardness of the coating. According to Archards equation, layer removal can be calculated using these relationships weighted by a wear coefficient k. In order to develop a function for the numerical determination of wear for the tests performed, an FE model of the test rig was created, which also accounts for the temporal and local effects relevant for wear.

3.4.1 Thermo-mechanical material characterisation for the numerical wear investigation

The anisotropy parameters for the Hill'48 model were determined based on the measured data regarding the change in width and length of the sheet specimens that were taken from the sheet in different orientations to the rolling direction. For the material DP600+Z the parameters F_1=0.462, G_1=0.564, H_1=0.436, N_1=1.366, L_1=1.5, M_1=1.5 and for the material DC04+ZE F_2=0.345, G_2=0.364, H_2=0.636, N_2=1.084, L_2=1.5, M_2=1.5 were identified. From the force displacement data of the experiments, plastic flow stress curves were determined. In each case, flow stress k_f was extrapolated up to an equivalent plastic strain value of ε_{eq} = 0.5 using the Hocket-Sherby approach, where, a, b, m and n are material and temperature dependent parameters:

$$k_f = b - (b - a)e^{-m\varepsilon_{eq}^n} \qquad (3\text{-}1)$$

The regression coefficients for the Hocket-Sherby approach of DP600+Z and DC04+ZE at the test temperatures are listed in Table 2.

Table 1: Temperature dependent regression coefficients of Hochet-Sherby approach for DP600+Z and DC04+ZE

	DP600+Z			**DC04+ZE**		
	20 °C	80 °C	120 °C	20 °C	80 °C	120 °C
a, MPa	0.388	0.368	0.295	0.2190	0.216	0.214
b, MPa	0.783	0.752	0.752	0.396	0.435	0.481
m	-13.4	-7.64	-5.06	-3.66	-1.91	-1.34
n	0.808	0.709	0.527	0.683	0.644	0.673

3.4.2 Numerical modelling of the wear tests

The numerical model of the strip drawing process as presented in chapter 2.2.3 was created in the commercial software environment Abaqus CAE 6.14-2. The basic configuration as well as the boundary conditions of the simulation model are shown in Figure 18 For further details see [2, 3]. Based on the results presented in [7], Coulombs friction model with a friction coefficient of μ = 0.1 was used, and 8-node hexahedral elements were employed to model the wear specimen.

Since it was assumed that the wear specimens do not undergo any plastic deformation, reduced integrated elements were used to minimise the computation time. In contrast, the sheet metal strip was meshed with deformable elasto-plastic shell elements. Five integration points along the thickness of the shell elements were used to model the bending movement over the cylindrical surface of the wear specimen. As the experimental wear tests were carried out at 80 °C with a sheet strip from DP600+Z, the corresponding material data (c.f. chapter 3) were used. Further model construction was based on the representative experimental data (c.f. chapter 2) using the specimens C and F.

Holding force

Specimen (elastic deformable)

Strip (elastic-plastic)

Tensile force
Displacement u = 60 mm
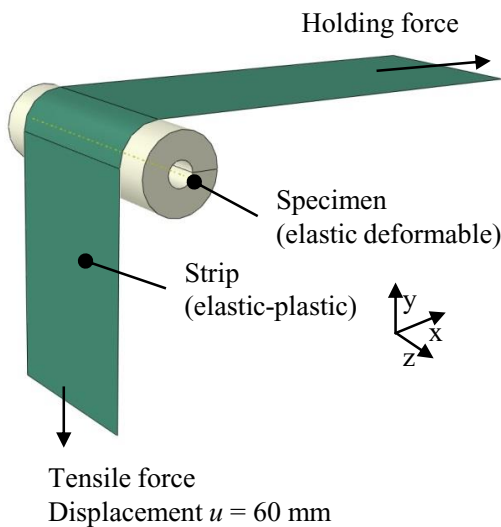
General boundary conditions
Abaqus CAE 6.14-2 standard FE solver
Coulomb friction model (friction factor μ=0.1)
Curves of holding force and strip velocity from experiments

Parameters of the specimen
8-node reduced integrated hexaeder elements (type: C3D8R)
Youngs modulus: 200,000 MPa; Poissons ratio: 0.3
Element edge length: 1 mm

Parameters of the strip
4-node reduced integrated shell elements (type: S4R)
Element edge length: 1 mm; element thickness: 1 mm

Figure 18: Schematic of the numerical model including FE-simulation parameters and boundary conditions for the strip-drawing test [8]

The relative slip rate in combination with the contact pressure is of great importance for the wear model developed in this study. Hence, instead of assuming an average slip rate value, the actual course observed in the relative movement of the strip and the wear specimen was modelled. Thus, the influences of the peak velocities at the corresponding contact pressures could also be included in the calculations. Figure 19a shows the velocity-time curve of the sheet metal strip during a cycle of the wear test on specimen C. The strip was first accelerated to a maximum speed of 70 mm/s before being slowed down again. The entire cycle lasted 1.54 s. It took about 0.4 s until the holding force of $F_h = 13,8$ kN was reached. Thereafter, the holding force was kept constant. The experimental data concerning velocity and holding force were introduced as boundary conditions into the simulation model. Table 3 shows the key parameters of the wear tests on specimen C and F.

Table 2: Holding forces from the different experimental setups with specimen C and F

Wear Specimen	Holding force F_h, N	Time needed to reach the maximum force, s
C	13822	0.40
F	15625	0.43

The models were validated by comparison of experimentally measured and numerically calculated force-displacement curves. As shown in Fig. 19b and c, there is good agreement of the force displacement curves between experiments and simulations, which indicates that the contact pressure was accurately calculated in the model.
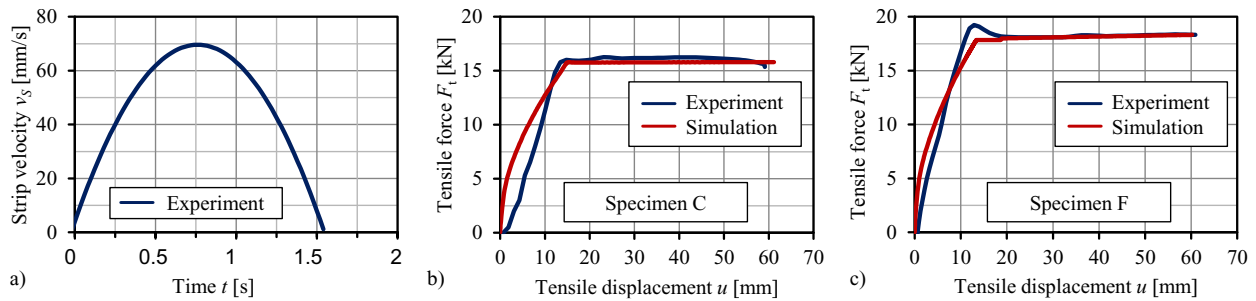

Figure 19: Validation of force displacement curves with different experimental setups for specimen C (b) and specimen F (c) along with the strip velocity-time profile throughout one cycle (a) [8]

For the subsequent investigation of the wear behaviour of the oxide layer, the load conditions for the specimens from the experimental series C and F were first examined numerically. It was found that the slip rate between sheet metal and specimen was quite uniform over the contact area in all cases. Consequently, it can be assumed that the wear rates determined in the investigations are mainly influenced by the local distribution of contact pressure. In turn, the different contact pressures are a result of the different holding forces of the metal strip from the experiments with specimens C and F (cf. Table 3). The calculated local contact pressures on specimen C are shown as an example in Figure 20Figure a.
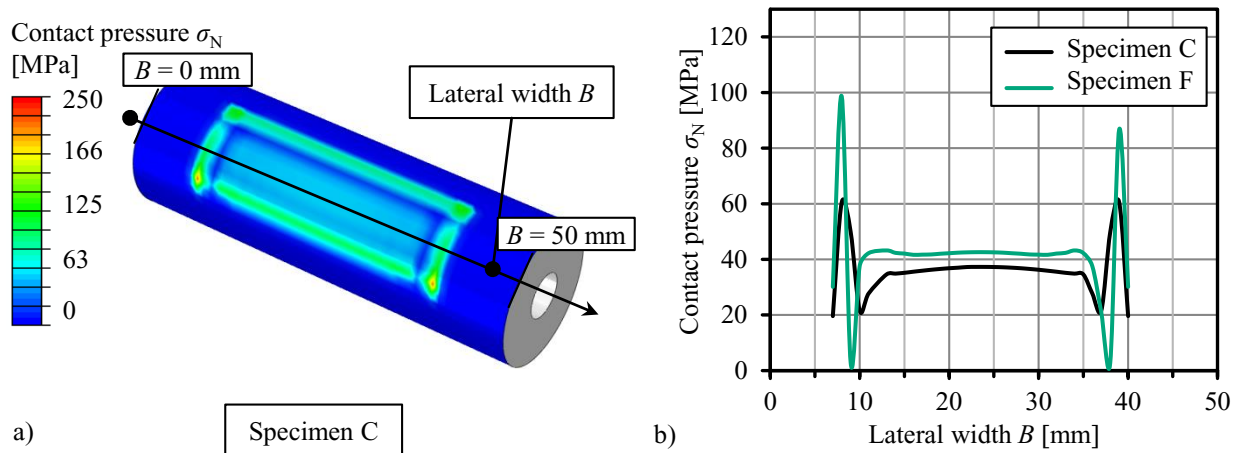

Figure 20: Contact pressure on the wear specimen C during the strip drawing test (a), comparison of contact pressure on the specimen C and F from different experimental setups (b) [8]

Increased contact pressures at the inlet and outlet areas of the sheet as well as increased contact pressures at the edge areas of the sheet strips characterise the contact pressure distributions calculated for all specimens. In contrast, the contact pressures on the remaining surfaces of the specimens are distributed fairly homogeneously. A comparison of the amount of contact pressure along the measuring line in lateral direction at an arc of contact from 45 ° is shown in Figure 20b. The characteristic stress distribution described above can be seen on both specimens. Therefore, only specimen C is discussed in the following. In the FIB analyses, a measuring point in the middle area of the specimen with a lateral width of 25 mm at an arc of contact of 45 ° was used to analyse the layer wear. In this way, the wear at the measuring point should be as uniform as possible over the entire cyclic tests, whereby side influences as well as run-in and run-out effects of the sheet strip can be neglected. In the next step, the wear function was developed on basis of the experimental results from the wear tests (cf. chapter 2).

3.4.3 Development of a function for calculating the wear of the α-Fe$_2$O$_3$ layer

The thickness of the initial layer as well as the remaining layer after different numbers of load cycles was determined by FIB analyses to determine the wear progress as a function of the number of cycles. Figure 21 summarises the results of these investigations. The wear of the layer shows a typical course depending on the cycle number as described in chapter 1. This course was interpolated with a polynomial function of fifth degree. The regression coefficients are given in the inset table in Figure . Based on the FIB data, the initial layer thickness was about 300 nm. This thickness was then reduced to ≈ 150 nm after 100 cycles. After this running-in phase the wear rate stabilises. In the range of 500 to 1000 cycles, only about 20 nm of the layer was removed. However, after 2000 cycles, the α-Fe$_2$O$_3$ layer could only be detected in isolated local places on the specimen. Thus, phase III of ablation, in which damage to the layer and the associated increased wear occurs, is reached before 2000 cycles. The starting point of phase III could not be determined exactly, as no measured values were available in this range. The wear polynomial used for this stage of abrasion has therefore to be regarded as a maximum estimate.

In order to calculate the wear, Archard's model was used. According to the general formulation of Archard's volume removal function, the incremental depth of wear Δw is calculated as

$$\Delta w = k \frac{\sigma_N}{H} v \Delta t \qquad\qquad (3\text{-}2)$$

In this formulation, the contact pressure σ_N, the slip rate v and the wear increment Δw are local and time dependent values. In the present study, a hardness H of 5600 MPa is used for the α-Fe$_2$O$_3$ layer, according to the previous investigations in [2].

The material specific wear coefficient k is an empirically determinable constant that is affected by the sliding direction of the process, the roughness of the friction bodies and other tribological influences.

As shown in chapter 1, the wear rate of a tool is subject to changes over its lifetime. For an improved prediction accuracy regarding the performance of the layer, an approach for the wear coefficient $k(n)$ depending on the number of cycles, n, is presented in equation 3-3. This equation consists of two interlaced sums. First, in a sum throughout all increments, the wear is accumulated according to the Archard equation as a function of σ_N, v and H for all of the time steps of duration Δt_i.
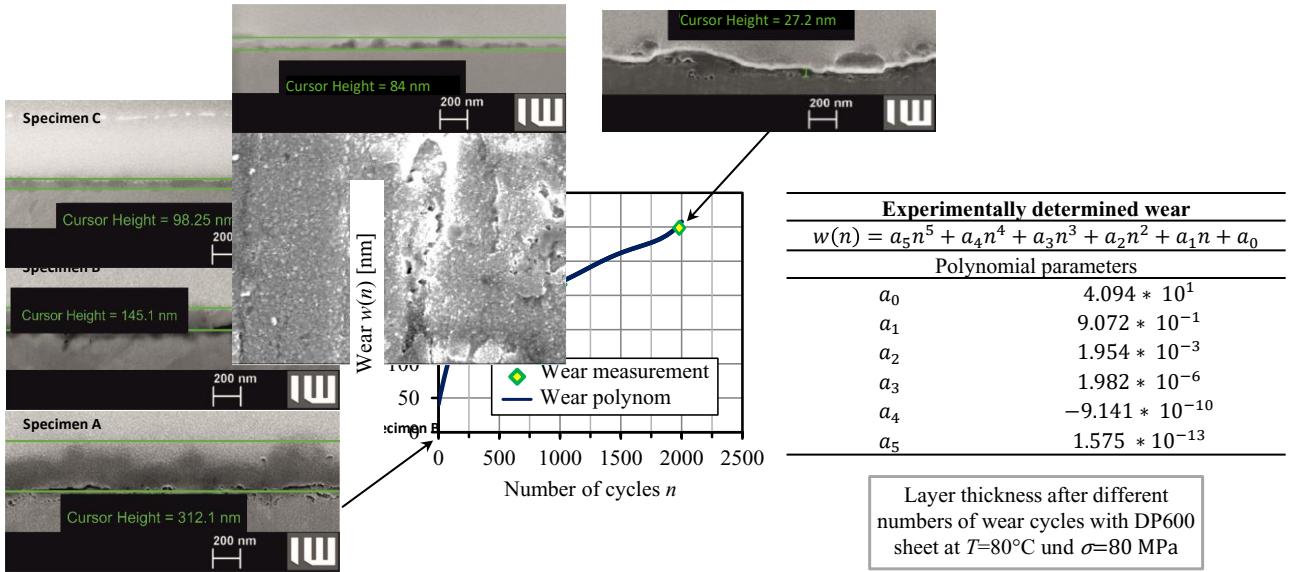
Experimentally determined wear	
$w(n) = a_5 n^5 + a_4 n^4 + a_3 n^3 + a_2 n^2 + a_1 n + a_0$	
Polynomial parameters	
a_0	$4.094 * 10^1$
a_1	$9.072 * 10^{-1}$
a_2	$1.954 * 10^{-3}$
a_3	$1.982 * 10^{-6}$
a_4	$-9.141 * 10^{-10}$
a_5	$1.575 * 10^{-13}$

Layer thickness after different numbers of wear cycles with DP600 sheet at T=80°C und σ=80 MPa

Figure 21: Experimentally determined wear from FIB analyses as well as parameters of the polynomial function for the wear with respect to the number of cycles of the α-Fe₂O₃ layer on specimen C [8]

This amount is subsequently offset against a cycle number-dependent wear coefficient k(n) for each wear cycle and the respective wear per cycle is accumulated.

$$w = \sum_{n=1}^{\text{Cycles}} \left\{ k(n) \sum_{i=1}^{\text{Increments}} \left[\frac{\sigma_N}{H} v \Delta t_i \right] \right\} \tag{3-3}$$

To determine a continuous function of the wear coefficients with respect to the number of cycles, equation 3-3 was mathematically reformulated as

$$k(n) = [w(n+1) - w(n)] \left\{ \sum_{i=1}^{\text{Increments}} \left[\frac{\sigma_N}{H} v \Delta t_i \right] \right\}^{-1} \tag{3-4}$$

From equation 3-4 in combination with the wear polynomial $w(n)$, the wear coefficient $k(n)$ was identified analytically using the calculation software Matlab. The results file of a strip drawing simulation contains the values of the contact pressure σ_N, the slip rate v and the incremental time Δt for all increments of one wear cycle. Using these data, the wear of one drawing cycle was calculated according to equation 3-3. This value equals the sum in equation 3-4. In combination with the polynomial $w(n)$ containing the coefficients from the table in Figure 21Figure , the wear factor could be calculated for each cycle number. The identified course of the wear factor $k(n)$ is shown in Figure 22 and is also given as a polynomial function with the coefficients listed in the inset table in Figure 22. This enables the model to predict the non-linear course of wear as a function of the current wear condition. Furthermore, the local contact pressure and the relative speed of the friction partners are also included in the calculation. The local contact pressure as well as the relative speed of the friction partners depend on the process-specific kinematics as well as on the material flow, thus the material parameters.
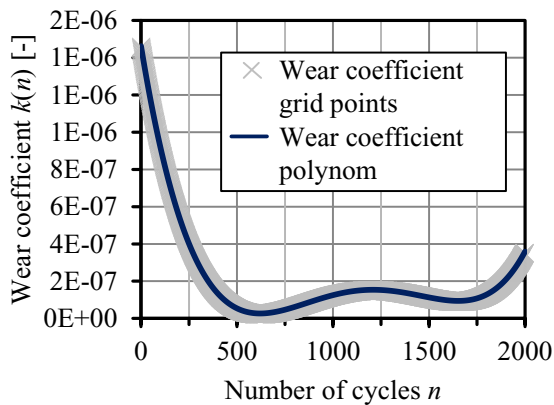
Numerically identified wear coefficien	
$k(n) = a_4 n^4 + a_3 n^3 + a_2 n^2 + a_1 n + a_0$	
Polynomial parameters	
a_0	$1.459 * 10^{-6}$
a_1	$-6.291 * 10^{-9}$
a_2	$9.576 * 10^{-12}$
a_3	$-5.892 * 10^{-15}$
a_4	$1.260 * 10^{-18}$

Figure 22: Numerically identified wear coefficient $k(n)$ from specimen C including polynomial coefficients

For the wear calculations, the results from the strip drawing FE models in Abaqus were modified by a python script in post processing using equation 3-3 including the numerically determined wear coefficient $k(n)$. Therefore, the wear distribution on the specimen surface can be calculated as a user-defined variable. Figure 23a illustrates the FE based calculated distribution of wear on the specimen C after 500 drawing cycles. Figure 23b shows a comparison of the experimentally measured and calculated wear values after different numbers of drawing cycles on the specimen C. After the model was calibrated using the wear data from specimen C, it was used to calculate the wear on specimen F after 500 cycles. The comparison of the experimentally measured and the calculated wear depth regarding specimen F is also shown in Figure 23b. It can be seen that the equation 3-3 implemented in the script with the help of the cycle number dependent wear factor provides good results for both the number of process cycles as well as the different contact pressure distributions resulting from the experimental boundary conditions.
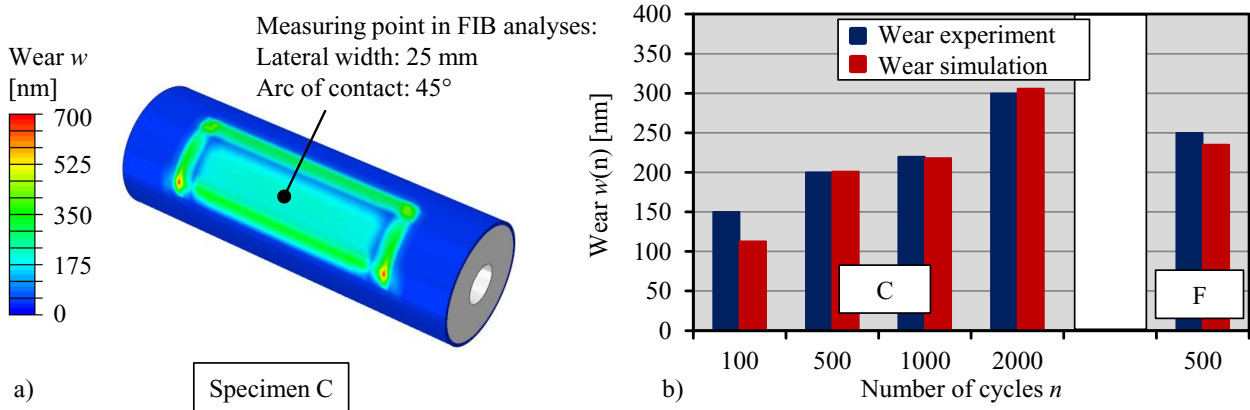

Figure 23: Wear on the specimen C after 500 cycles (a) and numerical results of wear on the specimen C and F after different numbers of cycles (b) [8]

3.4.4 Application of the developed numerical wear models to complex deep drawing processes

The experimental deep-drawing tests from chapter 3 were also numerically analysed focusing on the contact pressures and wear arising from different sheet materials. For this purpose, a three-dimensional FE quarter model was created in the Abaqus CAE 6.14-2 software. Tools like punch, blank holder and die were modelled as elastically deformable bodies. Therefore 8-node reduced integrated hexaeder elements with an average element edge length of 1 mm (type: C3D8R) were employed. The Young's Modulus was set to 200,000 MPa and Poisson's ratio to 0.3. The sheet material was modelled elastically-plastically deformable. In this case, 4-node reduced integrated shell elements with an average element edge length of 1 mm (type: S4R) were used, whereby the sheet thickness was set to 1 mm. As explained in [5], the friction coefficient between sheet and tool has been identified in experiments as $\mu = 0.1$. The data of the punch displacement and blank holder force were transferred from the experimental investigations to the simulation model. An isothermal process with a temperature of 80 °C was assumed.

At the top of Figure 24, the comparison of calculated von Mises stress σ_V distribution for the materials DP600+Z and DC04+ZE at a drawing depth of 50 mm is shown. The different stress values clearly illustrate the use of materials from two different strength classes. Accordingly, various contact pressures σ_N arise on the die in the two deep-drawing processes with DP600+Z and DC04+ZE (Figure 24, bottom). For both materials, the highest stresses occur in the corner areas of the die. Up to 397 MPa are locally present in the case of DP600+Z and up to 308 MPa in the case of DC04+ZE. In contrast, contact pressures are significantly lower on the longitudinal areas of the die. Here, an average contact pressure of 90 MPa was determined in the process with DP600+Z and 65 MPa with DC04+ZE. The amount of contact pressure on the longitudinal areas of the process with DP600+Z sheet metal is similar to the contact pressure on the specimens from the strip-drawing test shown in Figure 20a. This confirms the assumption made initially that the loadings in this area of the drawing die are similar to those in the strip-drawing test.
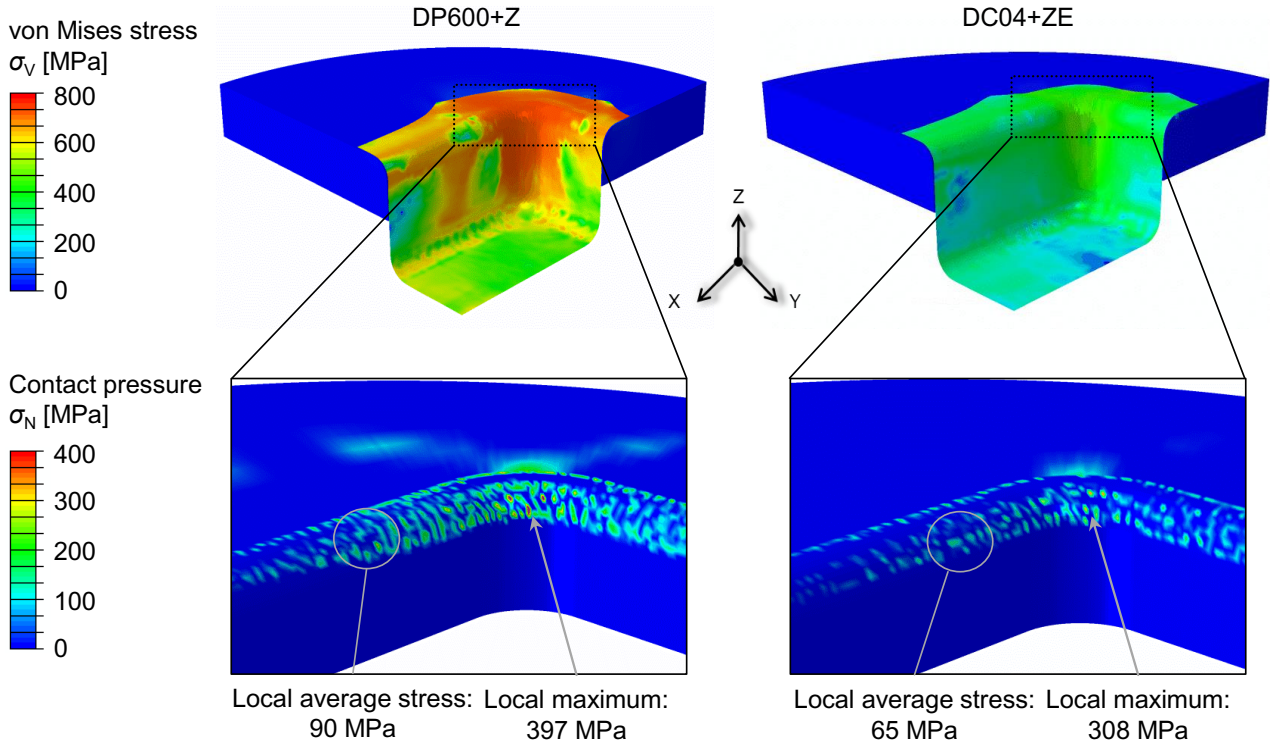
Figure 24: Von Mises stress in the deep-drawn sheet materials (top); contact pressure arising on the die due to the different sheet materials (bottom)

The script for calculating the layer wear was also applied to the complex deep-drawing processes. For the isothermal process temperature of 80 °C, the maximum number of cycles was calculated for the process with DP600+Z as 300 cycles and with DC04+ZE as 1450 cycles (cf. Figure 25). The wear critical area is in both cases the corner of the die. On the longitudinal sides of the dies, the wear is low. For the material DP600+Z, in this area an average wear of 180 nm was determined for the moment when the critical wear condition was reached in the corner area. For the material DC04+ZE, a similar wear of about 200 nm was calculated on the longitudinal side at this stage. It is noticeable that for the process with DC04+ZE a more uniform wear than for the process with DP600+Z was predicted, as the surface pressure is distributed more smoothly over the drawing ring during the deep drawing process. According to Figure 24, the local stress peaks are not as high as in the process with DP600+Z. Due to the higher strength of the sheet metal DP600+Z, higher stress peaks of 397 MPa are present in contrast to 308 MPa on the tool in the process with DC04+ZE. Thus, in the highly loaded areas of the tool in the process with DP600+Z, a locally faster wear is observed. Accordingly, the general wear criterion of this tool is reached earlier, which leads to the significantly lower number of maximum cycles of n = 300. Considering a certain point on the longitudinal side in the process with DP600+Z at an angle of 45 ° on the draw ring radius after 300 cycles, the calculated wear is about 150 nm. Since, as described above, the loads on the layer in this area are similar to those from the strip drawing tests, the wear calculated in this case appears plausible in the context of the calculated data in Figure 23b. Thus, it can be assumed that the developed wear model predicts the wear satisfactorily, and the model developed can be used as a numerical tool to predict the lifetime of the layer in actual application.

Furthermore, the influences of increasing process temperatures to 100 °C and 120 °C were investigated. The changed boundary conditions are modelled in the simulation by a temperature-dependent material flow behaviour. As expected, the increase in process temperature results in a minor increase of the maximum number of cycles. Accordingly, by increasing the process temperature from 80 °C to 120 °C, the maximum number of cycles increases by about 20 cycles for DP600+Z and by about 50 cycles for DC04+ZE.
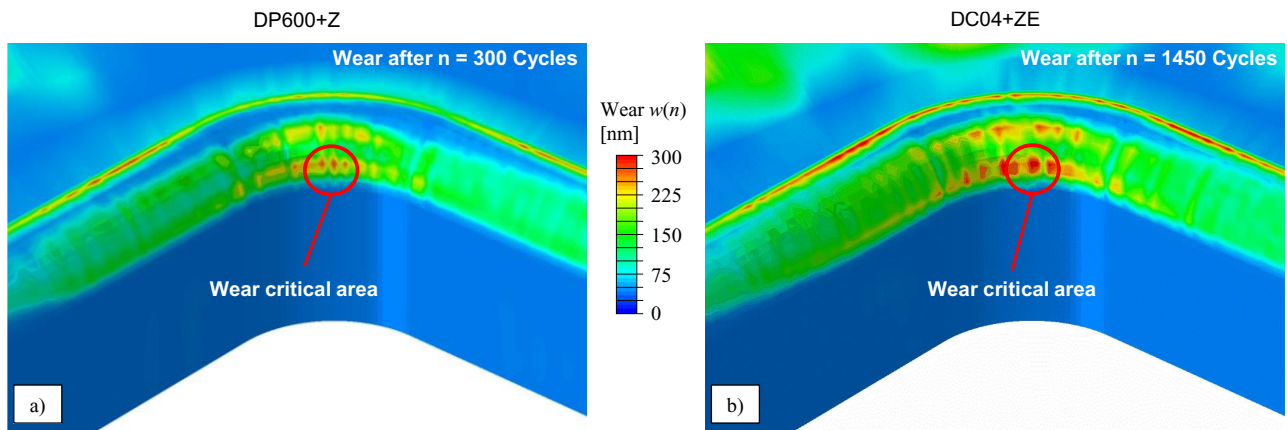
Figure 25: Prediction of the lifetime for the coating system during deep drawing of DP600+Z (a) and DC04+ZE (b) based on the wear critical areas using the developed wear function

3.5 Development of a deep drawing process with oxidised tool inserts

The results obtained demonstrated the potential of the layers realised via selective tool oxidation for dry metal forming. In an attempt to move closer to actual application, the focus of the final steps of this study was on forming tests and the production of three-dimensional components. In this context, a new modular deep-drawing tool with selectively oxidised inserts was developed and manufactured.

A rectangular cup geometry with a size of 160 mm x 80 mm was used for the deep drawing tests. Based on the numerical investigations, the areas in the rectangular cup that represent a high tribological load and surface pressure (longitudinal area and corner areas) were investigated. Thus, pockets were provided in the tool system at longitudinal and corner areas that could be fitted with oxidised and non-oxidised inserts. This allowed for testing different tool surface conditions without changing additional variables during the tests. Figure 26 shows an overview of the developed deep drawing tool with removable inserts.
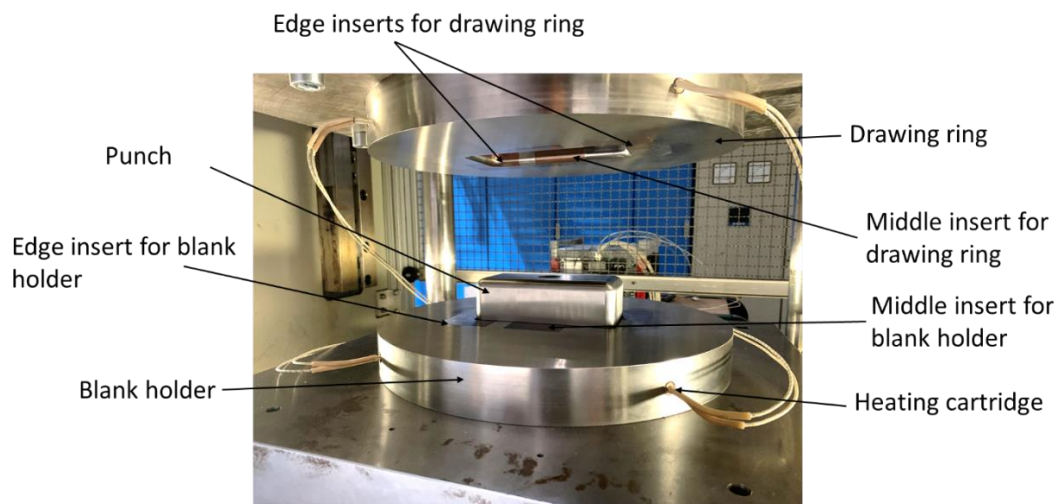

Figure 26: Overview of the deep drawing system using a modular tool concept

An electrolytically galvanised deep-drawing steel DC04+ZE and a hot-dip galvanised DP600+Z were used for the deep-drawing tests. In order to be able to compare the wear behaviour of the tool surfaces with each other, reference tests without an oxide layer were also carried out. The deep-drawing tests were performed for both sheet materials in the dry condition as reference, in the oxidised condition and in the oiled condition. Two different drawing depths (30 mm and 50 mm) were used for the sheet materials. Data about the deep-drawability were obtained by setting the drawing depth constant and continuously increasing the surface pressure.

3.5.1 Optical 3D-topography after deep drawing tests

In order to analyse the wear behaviour of the inserts, measurements were conducted similar to the wear tests described in chapter 2.2.3 before and after the deep-drawing tests in the area of the tool / work piece contact. Figure 27 shows the results of the 3D-profilometer roughness measurements of the different tool components. The surfaces of the inserts and the sheet metal used were tested. The deep-drawing forces for the individual tests were also recorded.
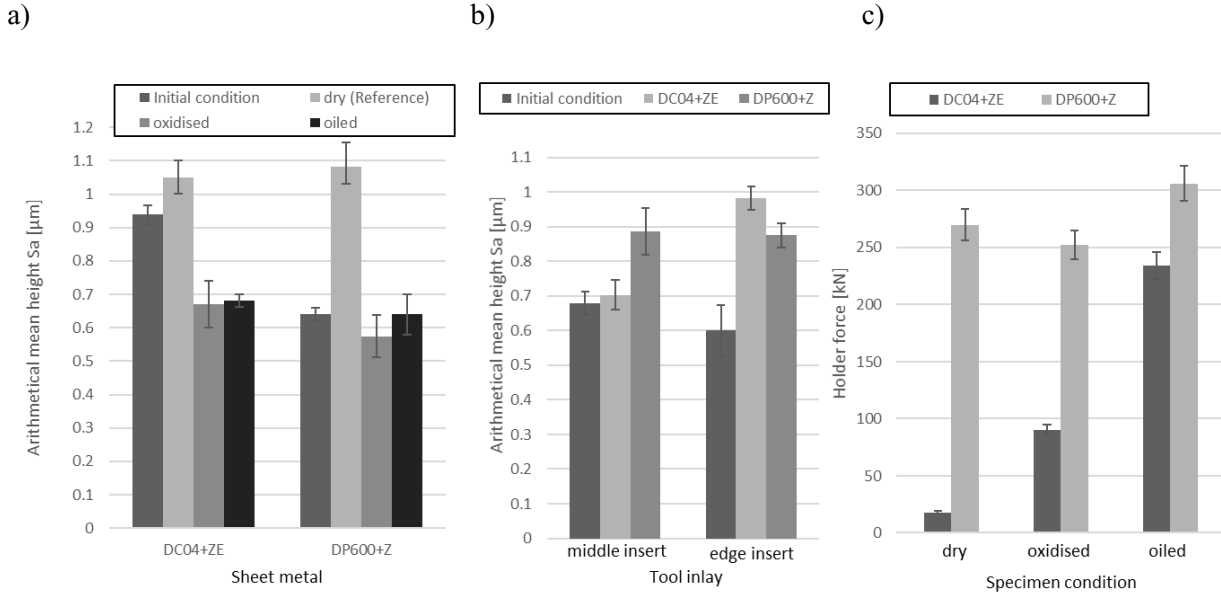
a)

b)

c)

Figure 27: Arithmetical mean height of the sheet surfaces with different conditions (a); arithmetical mean height of the inserts (b); blank-holder force depending on the sheet metals (c)

With a drawing depth of 50 mm, it was not possible to produce crack-free components when using the DC04+ZE. Thus, the investigations were continued at a drawing depth of 30 mm. As shown on the right of figure 27, the electrolytically galvanised sheet material DC04+ZE in dry condition has a reduced formability. The maximum possible blank holder force was 18 kN before component failure occurred. In contrast, four times higher blank holder forces were possible in the oxidised state (90 kN). By adding deep-drawing oil, the DC04+ZE could be deep-drawn very well. Here, the maximum possible blank holder force was 234 kN. In contrast, it is evident that the hot-dip galvanised sheet material DP600+Z can be deep-drawn in dry condition. Using this sheet material for both the dry and the oxidised state, blank holder forces of around 260 kN were achieved.

Depending on the sheet material used, the S_a-values varied. Figure 27 a) shows that the maximum S_a-values for DC04+ZE and DP600+Z were achieved in combination with the corner insert. In the initial state, the arithmetical mean height was 0.6 µm. After the deep-drawing tests were carried out, the S_a-value increased to 0.98 µm with DC04+ZE and to 0.87 µm with DP600+Z. A comparison of the S_a-values between the middle and corner inserts shows that the S_a-values of the middle inserts for DC04+ZE hardly increase. In contrast, the S_a-value of the DP600+Z is almost identical to the S_a-value of the corner insert. This is probably due to the increased zinc transfer from the DP600+Z to the surface of the inserts. After the tests were carried out, an increased zinc transfer from the DP600+Z was optically determined. In contrast, no zinc transfer was detected when using the electrolytically galvanised DC04+ZE.

In order to determine the changes on the insert surfaces after the deep-drawing tests, profiles of the surface were taken using a 3D-profilometer. Figure 28 (a and b) shows the surface of the middle and edge insert. The fine surface shows no optical defects or grooves. When comparing the tool surfaces from the process with DP600+Z, it is noticeable that the middle insert still shows a uniform pattern on the surface. The surface is similar to the undrawn insert. However, the surface of the corner insert looks different. In the lower drawing edge radius, first grooves are visible. This is also confirmed by the increased S_a-value in Figure 28 b. The bottom images (Figure 18 e) and f)) show the surface of the inserts that were drawn over with electrolytically galvanised DC04+ZE. It is noticeable that the surface of the corner insert shows clear defects and wear marks.

The striking surface structure of the corner insert in combination with DC04+ZE probably shows the lower deep drawability. During the tests with the sheet metal DC04+ZE, no zinc transfer to the insert surface could optically be detected.
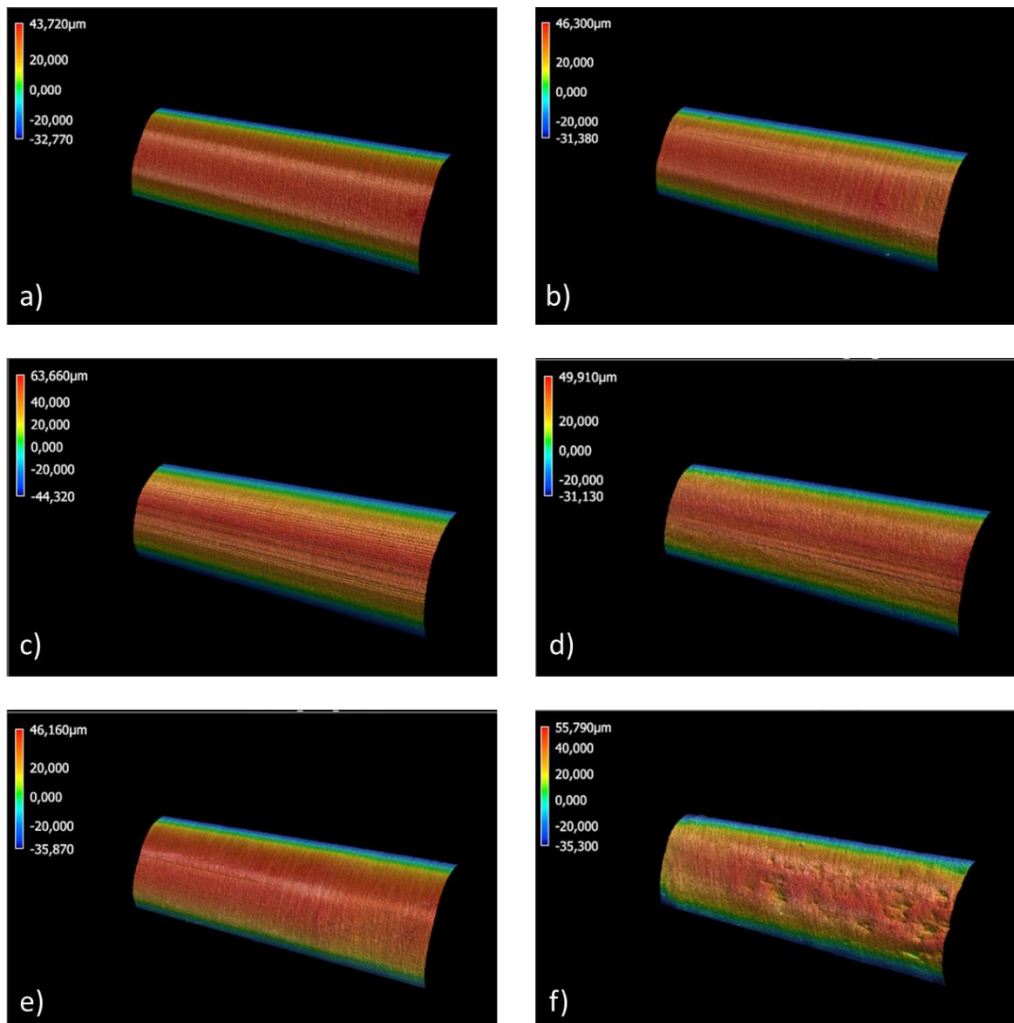

Figure 28: Surface images of inserts for deep-drawing tests; a) untested middle insert, b) untested edge insert, c) middle insert tested with DP600+Z, d) edge insert tested with DP600+Z, e) middle insert tested with DC04+ZE, f) edge insert tested with DC04+ZE

3.5.2 Analysis of the flange feed

Figure 29 shows the rectangular cups of the deep-drawing tests. As already mentioned, the different sheet materials were drawn with different drawing depths. Deep drawing of the DC04+ZE with the maximum drawing depth of 50 mm was not possible without failure. The enlarged pictures show the flange drawing of the deep-drawn samples. It is clearly visible that the flange feed was significantly increased for tools with oxidised inserts. The use of selectively oxidised inserts has resulted in a positive influence on the friction and wear conditions, particularly in the areas (corners) subject to higher loads. The improved friction conditions facilitated the material flow from the flange into the frame. In this way, premature material failure during forming could be prevented and formability was increased. This example shows that the selectively oxidised tool surfaces can have a positive influence on the resulting component quality.
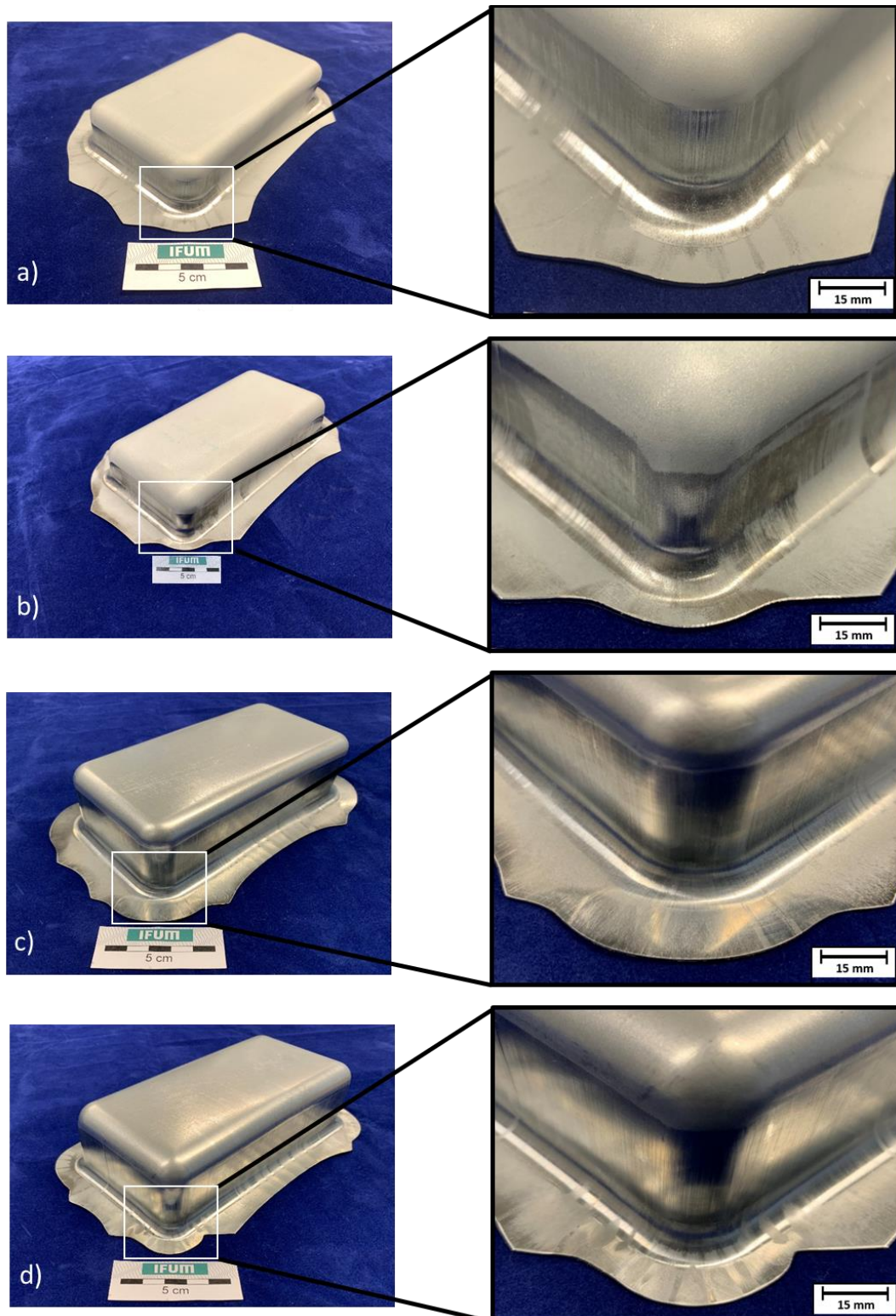
Figure 29: Deep-drawn rectangular cups; a) sheet metal DC04+ZE drawn over the reference surface, b) sheet metal DC04+ZE drawn over the oxidised surface, c) sheet metal DP600+Z drawn over the reference surface, d) sheet metal DP600+Z drawn over the oxidised surface

The rectangular cups from DC04+ZE shown in Figure 30 were both deep-drawn with the same process parameters. The rectangular cup, which was drawn over the non-oxidised (reference) insert, shows a crack in the corner area. In contrast, it was possible to produce components using the oxidised inserts. A less good deep-drawability results for the DC04+ZE, as no significant amount of zinc is transferred from the electrolytic zinc coating on the sheet surface to the insert surface. The absence of the zinc (separating layer) results in increased resistance in the contact area between sheet material and tool.
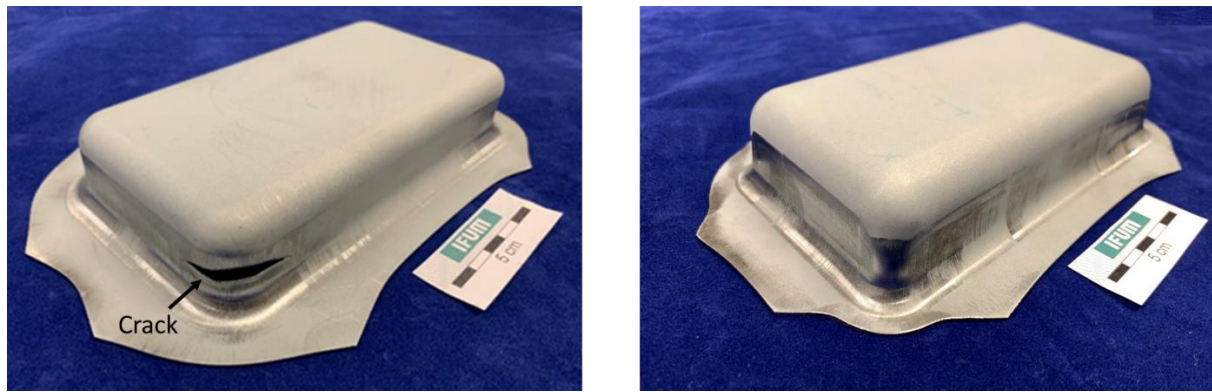
Figure 30: Rectangular cup (DC04+ZE) drawn over reference tool (left), rectangular cup (DC04+ZE) drawn over an oxidised tool

4   Summary and outlook

In the present study, dry metal forming was realised by heat treatment of tool steel surfaces resulting in the formation of selectively oxidised surfaces. The oxide layers generated acted as separation layers between tool and work piece in the dry sliding wear contact situations analysed. The heat treatment was conducted convectively and inductively to investigate different surface activations of hardened tool steel surfaces under defined temperature-time-regimes and atmospheres. After a detailed examination of different coating strategies, α-Fe_2O_3 oxide systems were chosen as separation layers. The challenging oxidation of the surface near chromium precipitations on hardened 1.2379 tool steel led to the use of PM tool steel surfaces, which featured more finely distributed chromium carbides at the surface. Thus, the generated layer systems also featured a higher adhesion strength on the PM tool steel surfaces. The data obtained in the wear tests were employed to develop a numerical model capable of simulating the material wear as a function of the process parameters. In this way, a deep drawing process could be simulated and the model was validated using a modular deep drawing tool. The results can be summarised as follows:

1. Using selective oxidation, α-Fe_2O_3 coating systems could be reproducibly generated on hardened tool steel surfaces.
2. Layers that were oxidised on PM steel surfaces provided higher adhesive strength than layers that were applied on conventionally produced hardened tool steel.
3. A batch process with an inductive heat treatment concept made it possible to oxidise the samples more efficiently via higher surface activation.
4. The oxidised layer systems generated had lower coefficients of friction than dry-tested tool surfaces.
5. The experiments demonstrated that selectively oxidised tool steel surfaces exhibiting α-Fe_2O_3 layers are suitable for decreasing wear during dry sheet metal forming. The transfer of adhesive zinc could also be reduced compared to non-oxidised surfaces.
6. Large chromium carbides present at the surface of the tool favour zinc transfer in this tribosystem.
7. The extension of the Archard model by a cycle number dependent wear coefficient demonstrated to be a suitable approach for the wear calculation of the α-Fe_2O_3 layers.
8. The numerical model developed allows predicting both overall tool life and local layer removal as a function of contact pressure, sliding velocity and the number of tool cycles.
9. Using a modular deep-drawing tool, processes with dry, oiled and oxidised tool surfaces could be realised.
10. The critical hold-down force for DP600 remained almost constant for all three conditions, indicating that DP600 + Z can be dry-drawn for small quantities. The high zinc transfer from the sheet to the tool plays a critical role in this process.

The use of oxidised tool surfaces appears promising for industrial applications. In the present study, all organic contaminants were carefully removed from the tools and deep-drawn sheets used. In this context, it is noteworthy that a factory pre-lubrication is usually applied on the deep-drawing sheets, which serves as a corrosion protection. Also not intended for use as a lubricant for deep-drawing, this could have a further positive effect on a deep-drawing process using selectively oxidised tools, in which no additional lubricants are used.

Acknowledgements

References

[1]   D. Wulff, D. Yilkiran, U. Holländer, D. Lützenkirchen-Hecht, R. Wagner, S. Hübner, K. Möhwald, H. J. Maier, B.-A. Behrens: Dry Selective oxidation of 1.2379 tool steel surfaces – an approach for Dry Metal Forming. Met. Forming OAJ FMT 1 (2015) 72-78

[2]   A. Almohallami, D. Yilkiran, D. Wulff, S. Hübner, M. Vucetic, H. J. Maier, B.-A. Behrens: Numerical Modelling of the Tribology of a Selective Oxidised 1.2379 Tool Steel Surface Developed for Dry Metal Forming. Dry Met. Forming OAJ FMT 1 (2015) 91-95

[3]   D. Yilkiran, A. Almohallami, D. Wulff, S. Hübner, M. Vucetic, H. J. Maier, B.-A. Behrens: New Specimen Design for Wear Investigations in Dry Sheet Metal Forming. Dry Met. Forming OAJ FMT 2 (2016) 62-66

[4]   D. Yilkiran, D. Wulff, F. Özkaya, S. Hübner, U. Holländer, H. J. Maier, B.-A. Behrens: Wear Testing of Thermally Oxidised Tool Steel Specimens with α-Fe$_2$O$_3$ Layers. Dry Met. Forming OAJ FMT 3 (2017) 45-49

[5]   D. Yilkiran, D. Wulff, A. Almohallami, F. Özkaya, A. Bouguecha A, S. Hübner, K. Möhwald, H. J. Maier, B.-A. Behrens: Wear behaviour of thermally oxidised tool surfaces as low-friction separation layers for dry sheet metal forming. Wear 376-377 (2017) 1789-1803

[6]   S. Schöler, D. Wulff, D. Yilkiran, B.-A. Behrens: Inductive heat treatment as an alternative tempering method for the selective oxidation of 1.2379 tool steel surfaces. Dry Met. Forming OAJ FMT 4 (2018) 13-17

[7]   S. Schöler, M. Schmieding, D. Yilkiran, F. Özkaya, C. Nowak, K. Möhwald, B.-A. Behrens, H. J. Maier: Wear behaviour of selectively oxidised α-Fe$_2$O$_3$ oxide low-friction layer systems on PM tool steel surfaces. Wear 426-427 (2019) 1603-1615

[8]   S. Schöler, C. Kock, F. Özkaya, C. Nowak, K. Möhwald, B.-A. Behrens, H. J. Maier: Numerical simulation of the abrasive wear behaviour of selectively oxidised α-Fe$_2$O$_3$ oxide layers on tool steel surfaces. JOM (2019)

[9]   F. Özkaya, S. Schöler, C. Kock, S. Hübner, B.-A. Behrens: Development of a tool concept with selectively oxidised inserts for dry deep drawing. Dry Met. Forming 5 OAJ FMT (2019) 46-49

[10] H. Czichos, K. H. Habig: Tribologie-Handbuch - Tribologie, Tribomaterialien, Tribotechnik 3rd edn. (2010)

[11] B.-A. Behrens, A. Bouguecha, B. Homann: (2013) Investigation of surface topography evolution of sheet aluminum under pressure and tension. Computational Plasticity XII (2013) 1230-1237

[12] G. Braeuer, H. Paschke, M. Weber, B.-A. Behrens, T. Yilkiran: Surface modifications for optimized forming operations. Key Engineering Materials (2014) 611-612 : 231-239

[13] B.-A. Behrens, A. Bouguecha, L. Lüken, J. Mielke, M. Bistron: Tribology in Hot Forging. Comprehensive Materials Processing 5 (2014) 211-234

[14] J. C. J. Bart, E. Gucciardi, S. Cavallaro (2013) Lubricants: properties and characteristics. Science and technology 1st edn. (2013) 27-29

[15] R. K. Hewstone: Environmental health aspects of lubricant additives. Sci. Total Environ. 156 (1994) 243-254

[16] F. Vollertsen, F. Schmidt: Dry Metal Forming: Definition, Chances and Challenges. International Journal of Precision Engineering and Manufacturing-Green Technology 1-1 (2014) 59-62

[17] D. Wulff, D. Yilkiran, U. Holländer, D. Lützenkirchen-Hecht, R. Wagner, S. Hübner, K. Möhwald, H. J. Maier, B.-A. Behrens: Selective oxidation of 1.2379 tool steel surfaces – an approach for Dry Metal Forming. Dry Met. Forming OAJ FMT 1 (2015) 72-78

[18] P. Groche, F. Resch: Dry forming of aluminium alloys - Wear mechanisms and influencing factors. Materials Science & Engineering Technology 46-8 (2015) 813-828

[19] A. Mousavi, A. Brosius: Tool concepts for dry forming. Dry Met. Forming OAJ FMT 1 (2015) 79-82

[20] M. Herrmann, C. Schenck, B. Kuhfuss: Dry Rotary Swaging with Structured Tools. Procedia CIRP 40 (2016) 653-658

[21] K. Bobzin, T. Brögelmann, A. Bastürk, F. Klocke, P. Mattfeld, D. Trauth: Development of an in situ Plasma Treatment of X155CRMoV12 for a (Cr, Al)N PVD Tool Coating for Dry Metal Forming in Cold Forging. Dry Met. Forming OAJ FMT 1 (2015) 57-62

[22] D. Yilkiran, D. Wulff, A. Almohallami, F. Özkaya, A. Bouguecha, S. Hübner, K. Möhwald, H. J. Maier, B.-A. Behrens: Wear behaviour of thermally oxidised tool surfaces as low-friction separation layers for dry sheet metal forming. Wear 376-377 (2017) 1789-1803

[23] V. B. Trindade, R. Borin, B. Z. Hanjari, S. Yang, U. Krupp, H.-J. Christ: High-Temperature Oxidation of Pure Fe and the Ferritic Steel 2.25Cr1Mo. Mater. Res. 8 (2005) 365-369

[24] R. Y. Chen, W. Y. S. Yuen: Review of the High-Temperature Oxidation of Iron and Carbon Steels in Air or Oxygen. Oxid. Met. 59 (2003) 433-468

[25] D. Wulff, U. Holländer, D. Lützenkirchen-Hecht, R. Wagner, D. Yilkiran, B.-A. Behrens, H. J. Maier (2015): Characterisation of selective oxidised steel surfaces by GIXRD. 11th DELTA User Meeting & Annual Report 2015 (2015) 70-71

[26] F. H. Stott, M.P. Jordan: The effects of load and substrate hardness on the development and maintenance of wear-protective layers during sliding at elevated temperatures. Wear 250 (2001) 391-400

[27] J. Glascott, F. H. Stott, G. C. Wood: The transition from severe to mild sliding wear for Fe-12%Cr-base alloys at low temperatures. Wear 97 (1984) 155-178

[28] J. Glascott, F. H. Stott, G. C. Wood: The effectiveness of oxides in reducing sliding wear of alloys. Oxid. Met. 24 (1985) 99–113

[29] J. Glascott, G. C. Wood, F. H. Stott: The influence of experimental variables on the development and maintenance of wear-protective oxides during sliding of high-temperature iron-base alloys. Proc. Inst. Mech. 199 (1985) 34-41

[30] F. H. Stott, M. P. Jordan: The effects of load and substrate hardness on the development and maintenance of wear-protective layers during sliding at elevated temperatures. Wear 250 (2001) 391–400

[31] J. Jiang, F. H. Stott, M. M. Stack: Some frictional features associated with the sliding wear of the nickel-base alloy N80A at temperatures to 250 °C. Wear 176 (1994) 185–194

[32] H. Kato, K. Komai: Tribofilm formation and mild wearby tribo-sintering of nanometer-sized oxide particles on rubbing steel surfaces. Wear 262 (2007) 36–41

[33] H. Kato: Severe–mild wear transition by supply of oxide particles on sliding
Surface. Wear 255 (2003) 426–429

[34] H. Kato: Effects of supply of fine oxide particles onto rubbing steel surfaces on
severe–mild wear transition and oxide film formation. Tribol. Int. 41 (2008) 735–742

[35] J.O. Edstrom: The mechanism of reduction of iron oxides. J. Iron Steel Inst. 175 (1953) 289–304

[36] V. B. Trindade, R. Borin, B. Z. Hanjari, S. Yang, U. Krupp, H. J. Christ: High-temperature oxidation of pure Fe and the ferritic steel 2.25Cr1Mo. Mat. Res. 8 (2005) 365-369

[37] J. S. Corneille, J.-W. He, D. W. Goodman: Preparation and characterization of ultra-thin iron oxide films on a Mo(100) surface. Surface Science 338 (1995) 211-224

[38] I. Milosev, J. M. Abels, H.-H. Strehblow, B. Navinsek, M. Metikos-Hukovic: High temperature oxidation of thin CrN coatings deposited on steel. J. Vac. Sci. Technol. A 14 (1996) 2527-2534

[39] J. M. Abels, H.-H. Strehblow: A surface analytical approach to the high temperature chlorination behaviour of Inconel 600 at 700°C. Corrosion Science 39 (1997) 115-132

[40] E. Clauberg, C. Uebing, H. J. Grabke: Surface segregation on Fe 25% Cr 2% Ni 0.1% Sb single crystals. Surface Science 433–435 (1999) 617-621

[41] E. Park, B. Hüning, M. Spiegel: Evolution of near-surface concentration profiles of Cr during annealing of Fe–15Cr polycrystalline alloy. Appl. Surf. Sci. 249 (2005) 127-138

[42] A. J. Davenport, M. Sansone, J. A. Bardwell, A. J. Aldykiewicz Jr., M. Taube, C. M. Vitus: In Situ Multielement XANES Study of Formation and Reduction of the Oxide Film on Stainless Steel. J. Electrochem. Soc. 141 (1994) L6-L8

[43] M. F. Toney, A. J. Davenport, L. J. Oblonsky, M.P. Ryan, C. M. Vitus: Atomic Structure of the Passive Oxide Film Formed on Iron. Phys. Rev. Lett. 79 (1997) 4282-4285

[44] G. Renaud: Oxide surfaces and metal/oxide interfaces studied by grazing incidence X-ray scattering. Surf. Sci. Rep. 32 (1998) 5-90

[45] L. G. Parratt: Surface Studies of Solids by Total Reflection of XRays. Phys. Rev. 95 (1954) 359-369

[46] G. Lim, W. Parrish, C. Ortiz, M. Bellotto, M. Hart: Grazing incidence synchrotron x-ray diffraction method for analyzing thin films. J. Mater. Res. 2 (1987) 471-477

[47] M. F. Toney, S. Brennan: Structural depth profiling of iron oxide thin films using grazing incidence asymmetric Bragg x-ray diffraction. J. Appl. Phys. 65 (1989) 4763-4768

[48] M. F. Toney, S. Brennan: Observation of the effect of refraction on X-rays diffracted in a grazing-incidence asymmetric Bragg geometry. Phys. Rev. B 39 (1989) 7963-7966

[49] A. Almohallami, M. Arghavani, F. Böhmermann, H. Freiße, M. Herrmann, S. A. Mousavi, S. Schöler, P. Scholz, J. Tenner, M. Teller, G. Umlauf, D. Wulff, D. Yilkiran, H. J. Maier: How dry is dry? A critical analysis of surface conditions used in dry metal forming. Dry Met. Forming OAJ FMT 3 (2017) 90-94

[50] C. Broennimann, E. F. Eikenberry, B. Henrich, R. Horisberger, G. Huelsen, E. Pohl, B. Schmitt, C. Schulze-Briese, M. Suzuki, T. Tomizaki, H. Toyokawa, A. Wagner: The PILATUS 1M detector. J. Synchrotron Radiat. 13 (2006) 120–130

[51] P. Kraft, A. Bergamaschi, C. Broennimann, R. Dinapoli, E. F. Eikenberry, B. Henrich, I. Johnson, A. Mozzanica, C. M. Schlepütz, P. R. Willmott, B. Schmitt: Performance of single-photon-counting PILATUS detector modules. J. Synchrotron Radiat. 16 (2009) 368–375

[52] D. Lützenkirchen-Hecht, R. Wagner, S. Szillat, A. K. Hüsecken, K. Istomin, U. Pietsch, R. Frahm: The multi-purpose hard X-ray beamline BL10 at the DELTA storage ring. J. Synchrotron Radiat. 21 (2014) 819–826

[53] M. Tolan, T. Weis, K. Wille, C. Westphal: DELTA: synchrotron light in Nordrhein-Westfalen. Synchrotron Rad. News 16 (2003) 9–11

[54] Guideline VDI (Association of German Engineers) 3198: Beschichten von Werkzeugen der Kaltmassivumformung. CVD- und PVD-Verfahren

[55] J. F. Archard: Wear Theory and Mechanism. Wear Control Handbook (1980) 35-80

[56] K. Ersoy, M. Labermeyer: Verschleiß sicher vorhersagen. Blech InForm 3 (2007) 90-93

[57] B.-A. Behrens, A. Bouguecha, M. Vucetic, A. Chugreev: Advanced Wear Simulation for Bulk Metal Forming Processes.